



# PROFESSORSHIP OF DIGITAL SIGNAL PROCESSING AND CIRCUIT TECHNOLOGY

## RESEARCH PROJECT

### **From Points to Images: Transformation of single planes to binary images**

*Raul Beltrán B.*

supervised by  
M.Sc. Roman SEIDEL



# R Research Project

- 1. Motivation**
- 2. Main Task**
- 3. State-of-the-art**
- 4. Methods**
  - 4.1. 3D space to 2D plane**
  - 4.2. Thresholding and Morphological Filtering**
  - 4.3. 2D to 3D Mapping**
- 5. Experiments**
- 6. Results**
- 7. Evaluation and Outlook**
- 8. References**

## R 1. Motivation

- Indoor Positioning Systems (IPS) is a growing up technology that enables a multitude of new user experiences.
- IPS produces an important amount of data to characterize the behaviour of people, places or objects.
- GPS signals for indoor environments still is a difficult problem; bad reception and multi-path fading limit the precision. [1]
- Chair DST at TU-Chemnitz works with 3D-modeling scenes based on omni-directional sensors to get full hemispherical depth information from an indoor space. [2]
- Previous research worked with a noisy 3D point cloud of a real scene; there walls and ground plane were extracted. [3]



**Figure 1.** Left and right images for stereo computation. Courtesy of chair DST, TU-Chemnitz.

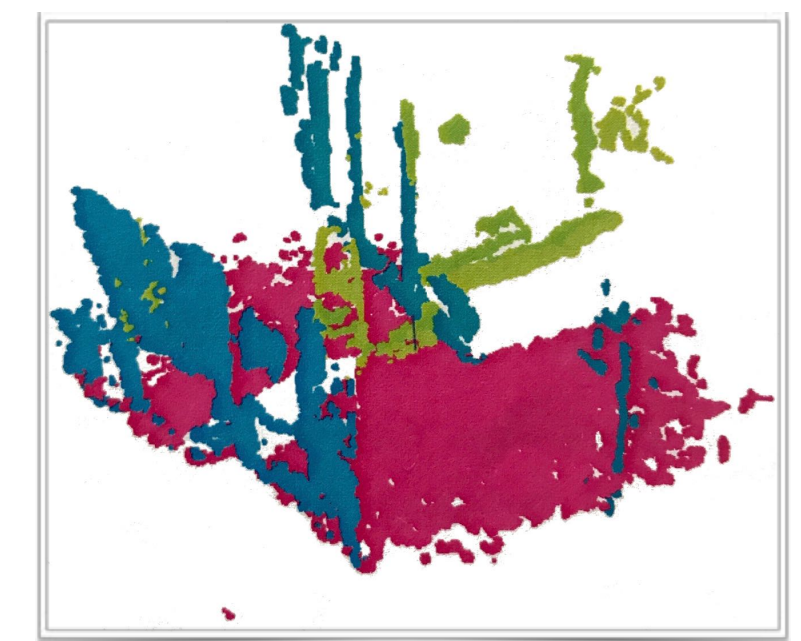


**Figure 2.** Planes extracted from a real indoor scene. [3]



## 2. Main Task

Given a noisy 3D point cloud model of a real scene, the main goal is to extract and reconstruct the ground plane.

- Transformation of the single planes of an indoor scene into binary images.
- Application of morphological operators to improving the quality of each plane.
- Back-transformation of the reconstructed plane of the floor to a point cloud.

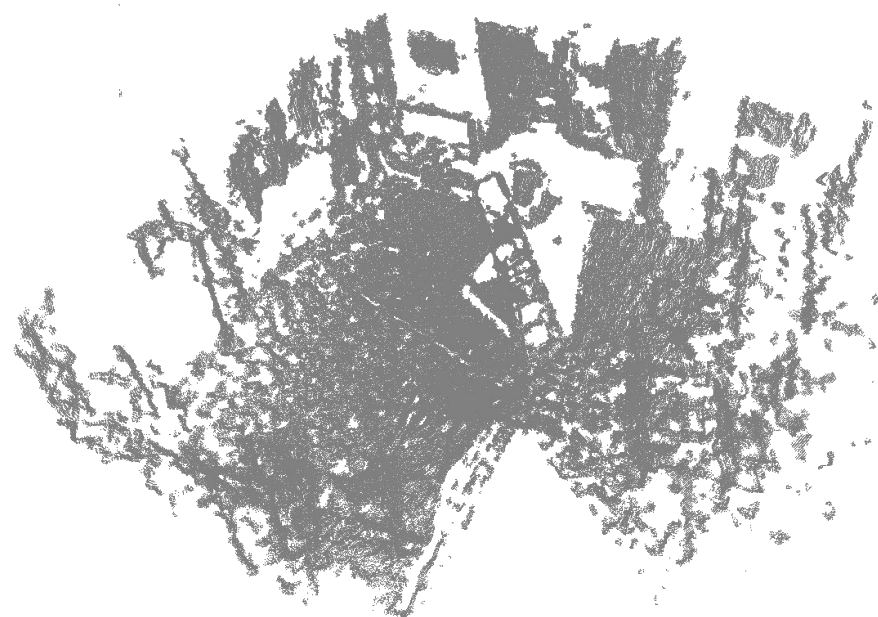


**Figure 3.** Point cloud generated from two fisheye images.

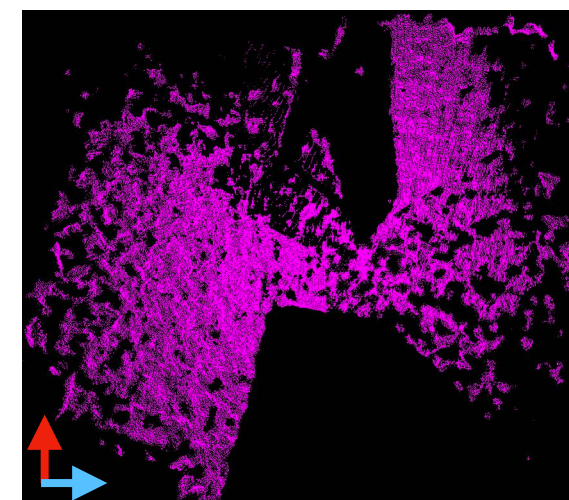


**Figure 4.** Ground plane plane extracted by RANSAC. [3]

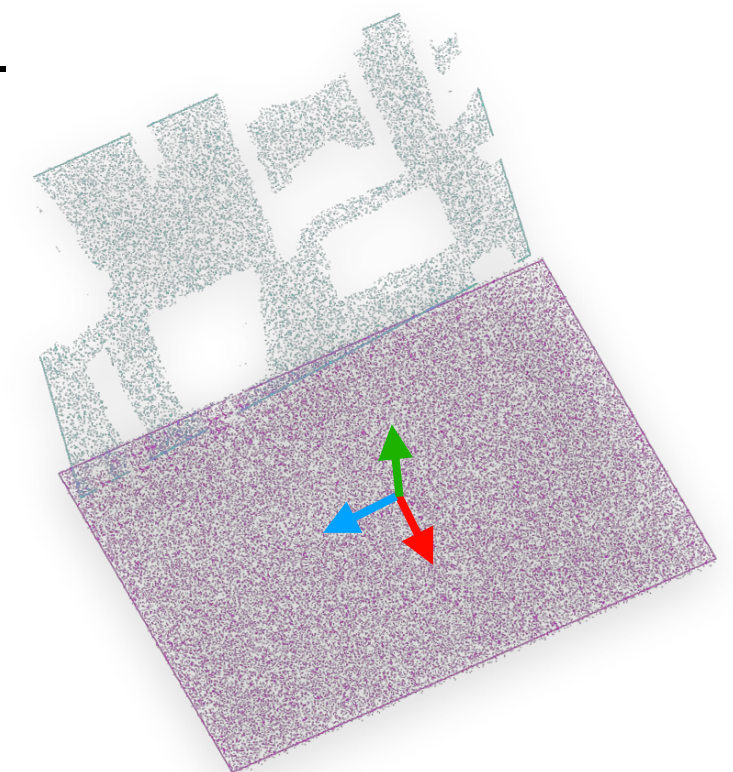


**Figure 5.** Point cloud to reconstruct and back-transform to the 3D space.



## 2. Main Task

Given a noisy 3D point cloud model of a real scene, the main goal is to extract and reconstruct the ground plane.

- 3D → 2D transformation of points into a binary image based on homogeneous coordinates.
- Use of thresholding and morphological filtering.
- Boundary extraction and plane shape reconstruction.
- 2D-image to 3D space mapping.



**Figure 3.** Point cloud generated from two fisheye images.



**Figure 6.** 2D-image of the ground plane to apply it morphological operators.

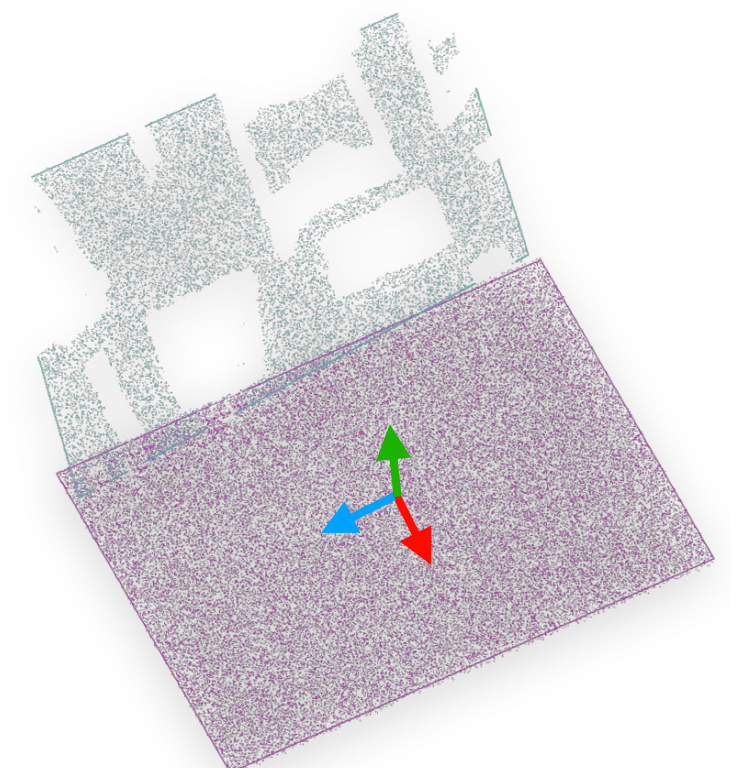


**Figure 5.** Point cloud to reconstruct and back-transform to the 3D space.

## ⌚ 3. State-of-the-art

- Digitization process → Acquisition and Recording partial views. [4]
- Stereo computation → Imaging Process, Stereo Correspondence Computation, Triangulation and Spherical Distance Map Generation. [2]
- Gaps appear due to multitude of parameters from acquisition to post-processing. [6]

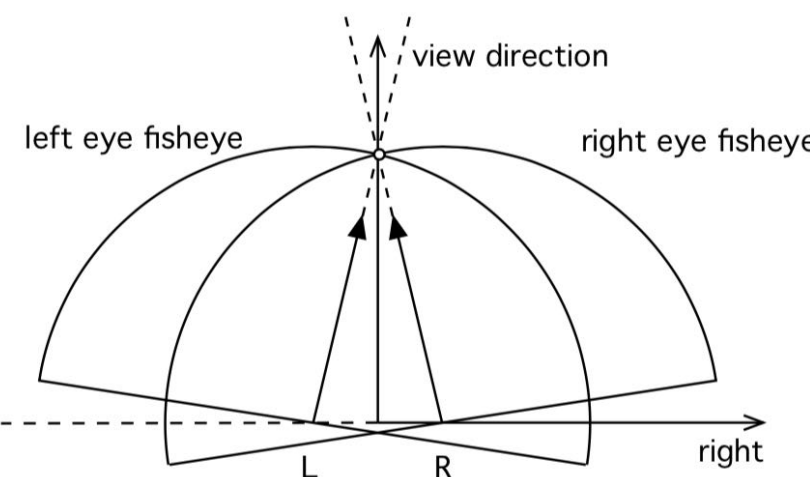


**Figure 7.** Stereoscopic projections based upon a pair of toe-in fisheye projections. [5]



**Figure 8.** Image from a trinocular configuration. Courtesy of chair DST, TU-Chemnitz.

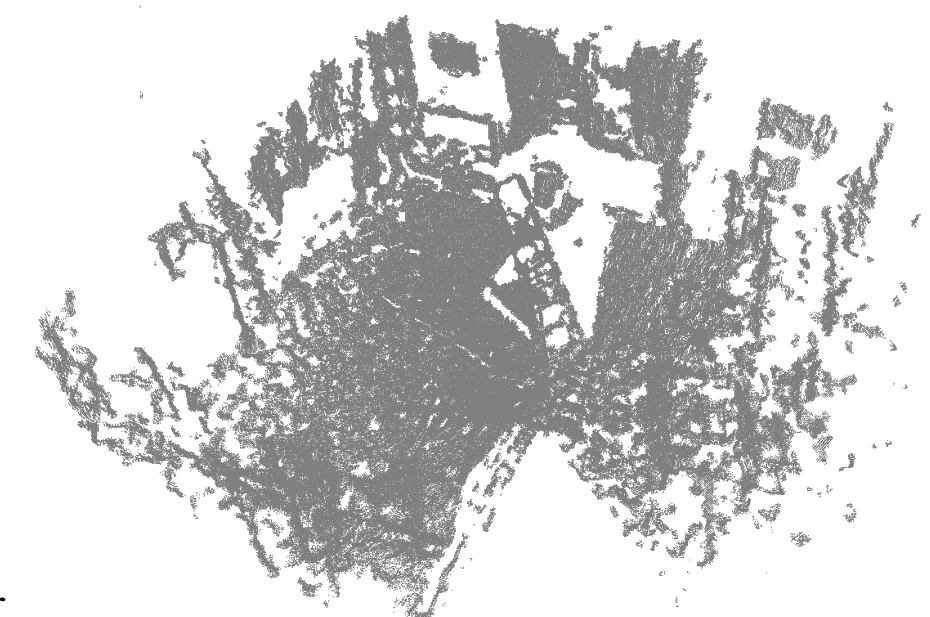


**Figure 3.** Point cloud generated from two fisheye images.

## 3. State-of-the-art

- In the mapping of a static indoor scene there is a minimal assumption:  
**exist walls and a ground area.**
- To extract regular geometric shapes from point clouds three main lines of research can be identify: [7] [13]
  - Approaches based on RANSAC (Random Sample Consensus) algorithm.
  - Methods using the Hough transform.
  - Algorithms that use region growing.
- Contour detection algorithms can be classified by the perceptually importance of the features used: [8]
  - Local methods, where luminance, colour and texture are the defining features.
  - Global methods, where the contours are recognized on good continuation and closure.
- The value used for thresholding determines the quality of the output. Methods such Otsu automatically choose this value. [9]

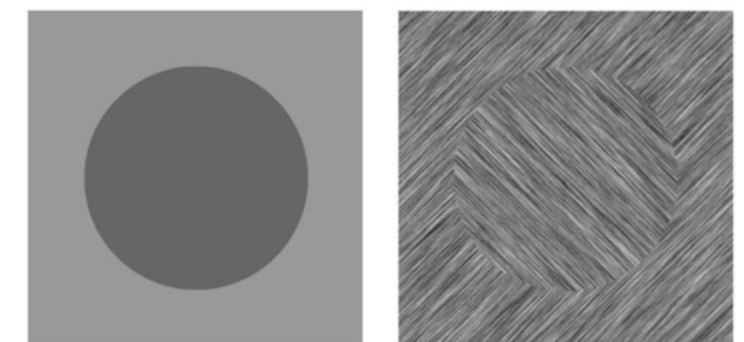


Figure 9 illustrates four contexts related to contour perception:

- a) Luminance: A solid gray circle is perceived as a circle due to its uniform luminance against a textured background.
- b) Texture: A textured surface with diagonal stripes is perceived as having a smooth boundary due to the grouping effect of similar textures.
- c) Perceptual grouping: Four small black semi-circles arranged in a square pattern are perceived as a complete circle, demonstrating the principle of grouping by proximity and similarity.
- d) Illusory contour: Two black semi-circles with a white space between them are perceived as a complete circle, illustrating the concept of illusory contours formed by good continuation and closure.

**Figure 9.** Some contexts to contours perception: a) luminance, b) texture, c) perceptual grouping, and d) illusory contour. [8]

## 3. State-of-the-art

- Similarities exist between the image restoration algorithms and the problem of filling gaps in 3D surfaces. [4]
- Efficient and robust calculation of the projection is essential for: [10]
  - Calculating the nearest point (landmark) in a curve or surface
  - Parameter estimation of a point in space
  - Calculation of intersection and similarity.

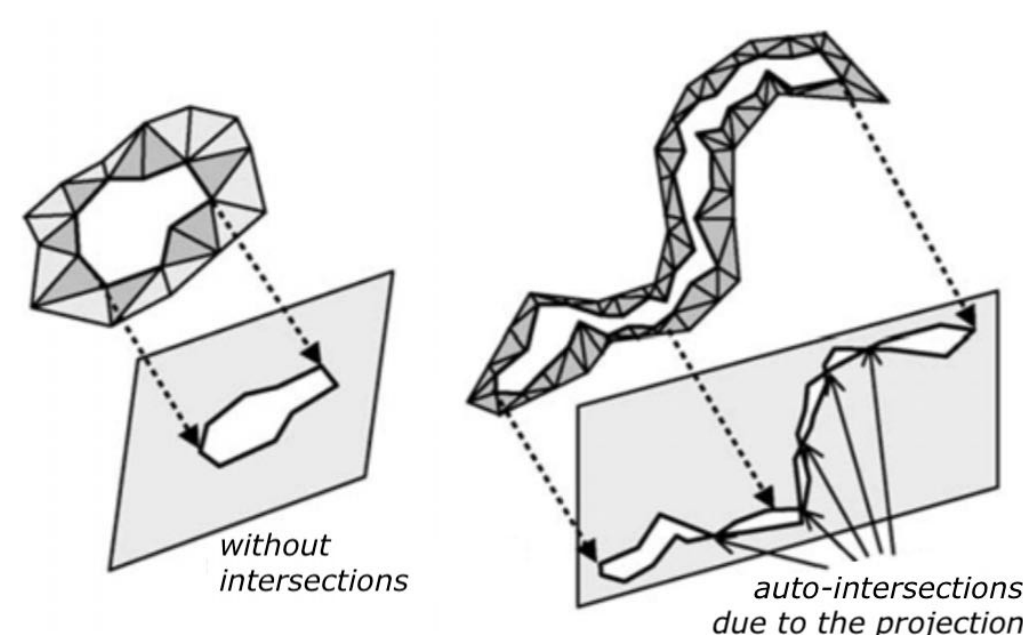


**Figure 10.** Projection of polygonal holes in a plane. [4]



## 4.1. Methods - 3D space to 2D plane

- In a homography the projected figure is equivalent to the original, leaving points as points and mapping lines to lines.
- The most specialized transformation of the projectivities in  $\mathbb{R}^2$  is the isometry, where the Euclidean distance is preserved. This is specially useful to model the motion of a rigid object.  
[11]

$$\begin{pmatrix} x' \\ y' \\ 1 \end{pmatrix} = \begin{bmatrix} \epsilon \cos \theta & -\sin \theta & t_x \\ \epsilon \sin \theta & \cos \theta & t_y \\ 0 & 0 & 1 \end{bmatrix} \begin{pmatrix} x \\ y \\ 1 \end{pmatrix} \quad (1)$$

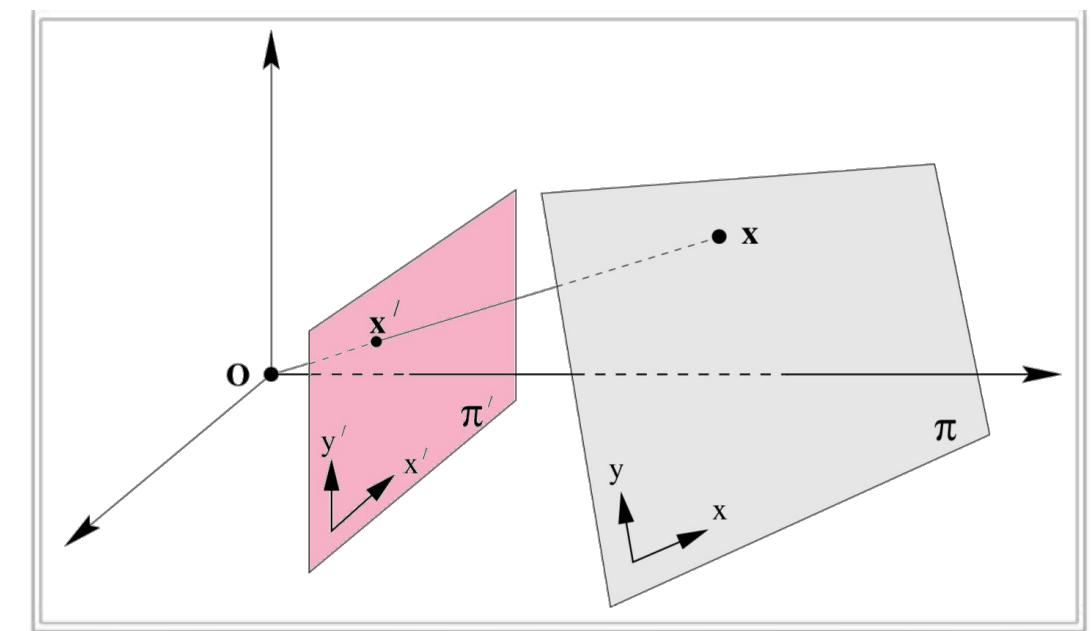


**Figure 11.** Linear transformation on  $\mathbb{R}^3$  mapping two planes along a single ray.

Or, in its block format representation:

$$X' = H_E X = \begin{bmatrix} R & t \\ 0^T & 1 \end{bmatrix} \quad (2)$$



## 4.2. Methods - Thresholding and Morphological Filtering

- Thresholding 2D presents better results in the segmentation of affected images with noise. [9]
- Mathematical morphology. Tool used to extract components of the image useful in the representation and description of the shape. [12]

For a set  $A$  and a structuring element  $B$ , it is defined:

$$\text{Erosion: } A \ominus B = \{x \in E^n \mid (B)_x \subseteq A\} \quad (3)$$

$$\text{Dilation: } A \oplus B = \{a \mid (B)_a \cap A = \emptyset\} \quad (4)$$

$$\text{Opening: } A \circ B = (A \ominus B) \oplus B \quad (5)$$

$$\text{Closing: } A \bullet B = (A \oplus B) \ominus B \quad (6)$$

- The morphological operators are used to obtain the contour of an object; internal or external depending on the used method.
  - Morphological gradient.
  - The hit-or-miss transformation.
  - Convex Hull.



**Figure 12.** Gradient thresholding of the binarized image in Figure 8.

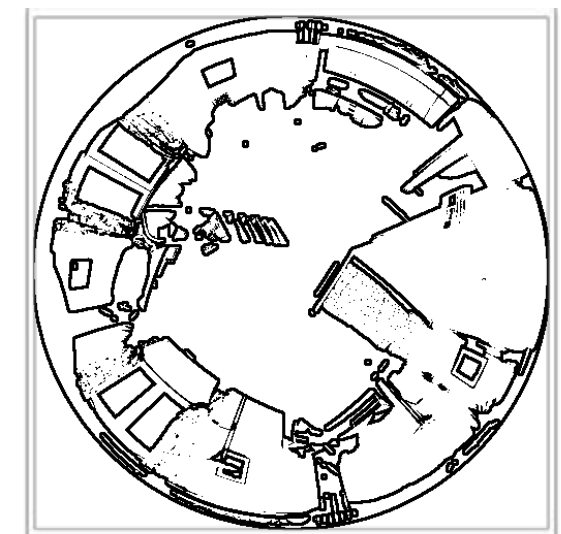


**Figure 13.** Inner contour obtained by the operation  $A - (A \ominus B)$ .



## 4.3. Methods - 2D to 3D Mapping

- To recreate the 3D mapping of an object from a 2D model it is necessary project to the space the control points from each planar parameterization. [10]

If a defined line  $L(\lambda) = \lambda A + (1-\lambda)C$  intersects the plane  $\pi$ , then

$$P_{PP} = \begin{bmatrix} \lambda A_x + (1-\lambda)C_x \\ \lambda A_y + (1-\lambda)C_y \\ \lambda A_z + (1-\lambda)C_z \end{bmatrix}^T \quad (7)$$

- Solution given by the inverse of the homography (Equation 2):

$$X = H^{-1}X' = \begin{bmatrix} R^T & -t \\ 0^T & 1 \end{bmatrix} \quad (8)$$

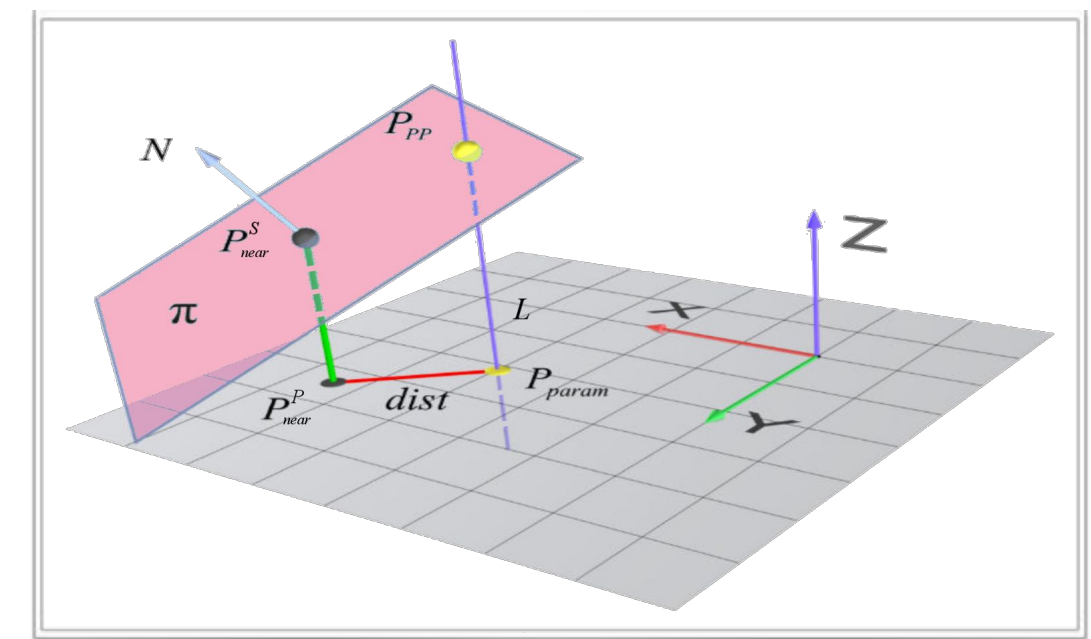


**Figure 14.** Scheme of point-to-point projection, from 2D-image to 3D space. Here  $P_{param}$  is a control point and  $P_{near}$  is the point to back-transform.

## ⚙ 5. Experiments

**Input data:**

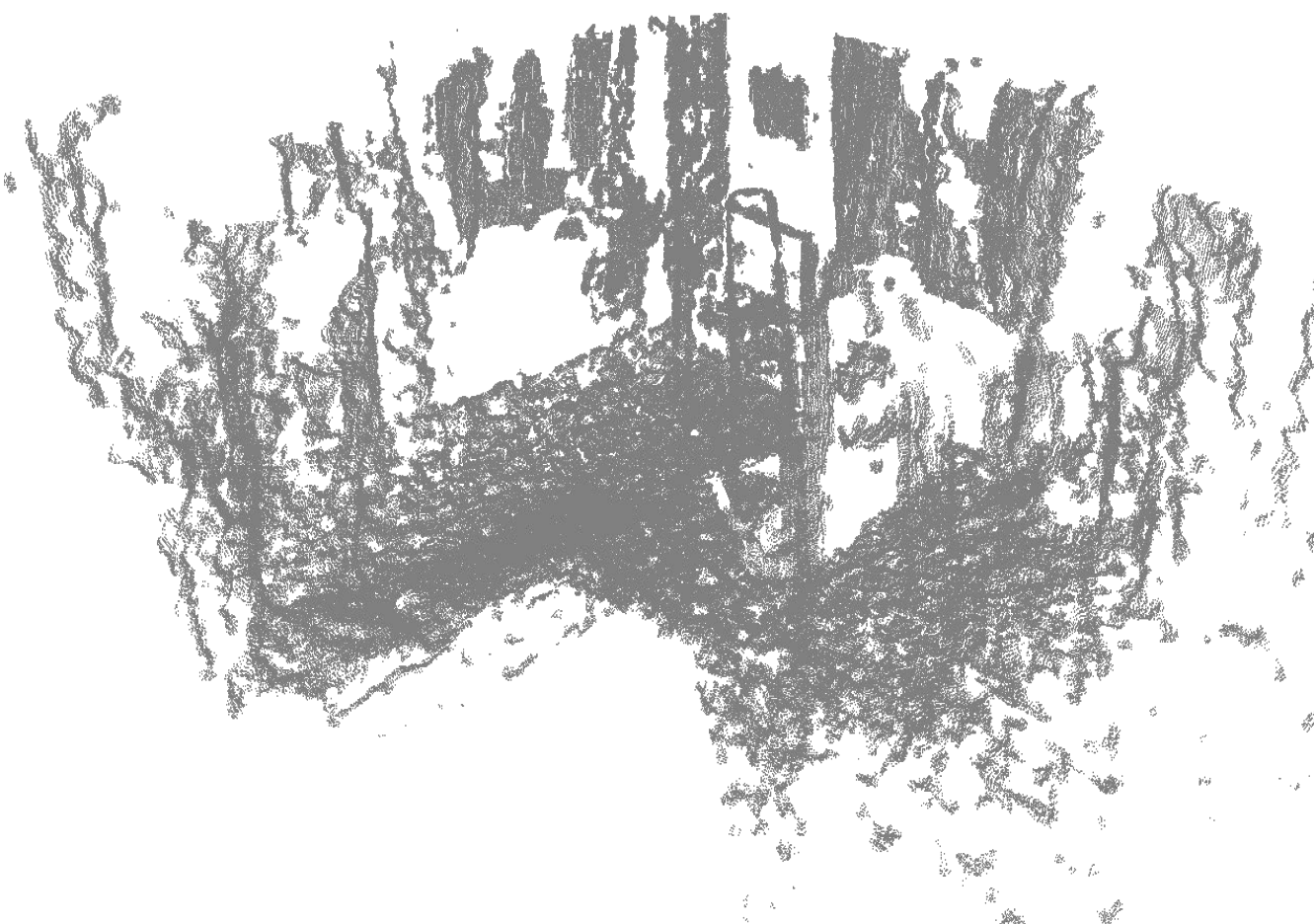


**Figure 15.** Point cloud generated from two fisheye images.

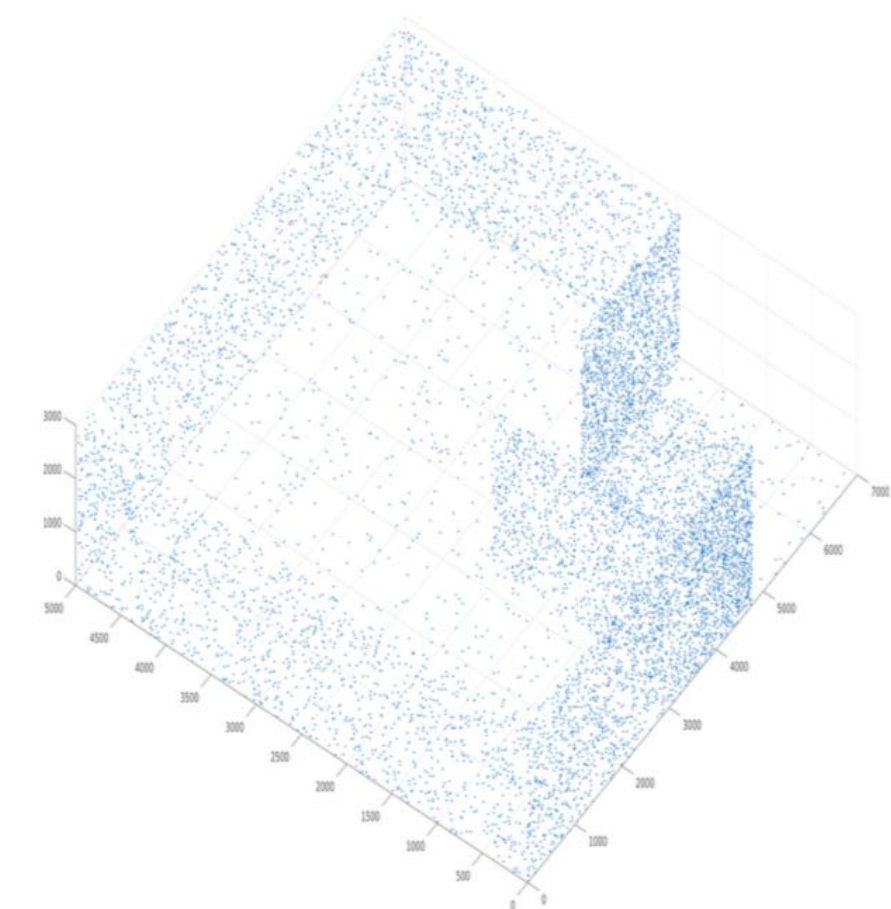


**Figure 16.** Synthetic construction of the scene for evaluation of the result. Courtesy of chair DST, TU-Chemnitz.

## ⚙ 5. Experiments

**Objective:** Estimation of 3D planes from a noisy point cloud with RANSAC.

- Two important variables to run a RANSAC: the threshold distance  $d$  and the epsilon angle  $\varepsilon$ . [3]
- Extraction of all possible planes per best-fit mode. Based on a cube model, only the outer planes are selected in each axis.

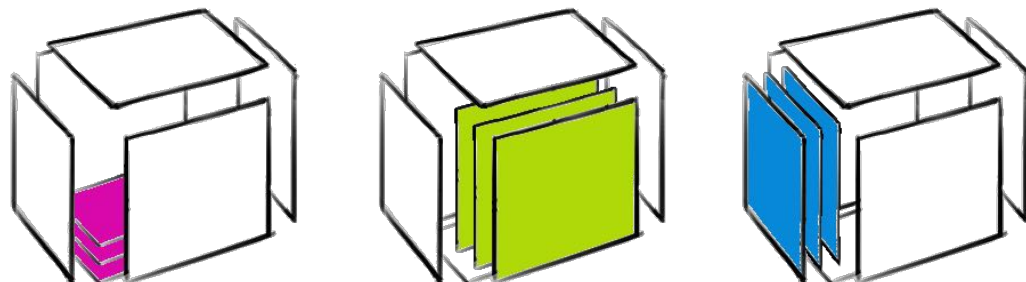


**Figure 18.** Iterative extraction of planes in  $z$ -,  $x$ - and  $y$ -coordinates.

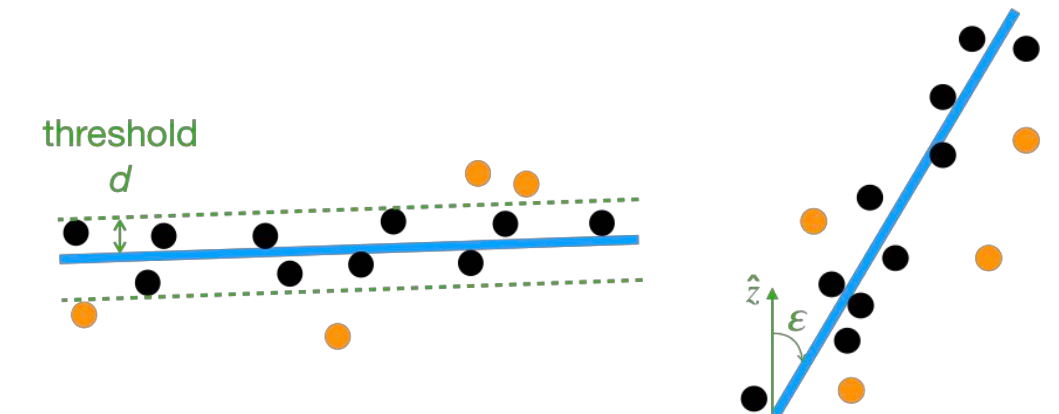


**Figure 17.** Parameters  $d$  and  $\varepsilon$  over the estimated plane.

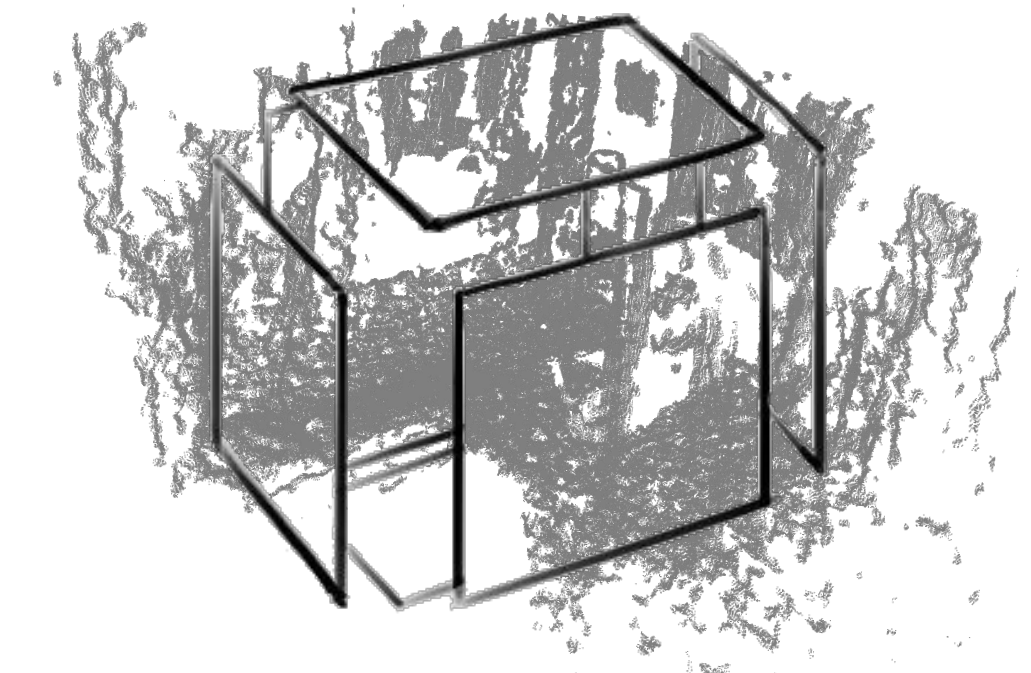


**Figure 15.** Given point cloud of the room scene.

## ⚙ 5. Experiments

**Objective:** Analytical calculation of the ground plane limits by wall planes intersection.

- Given the planes  $X, X', Y$  and  $Y'$ , it is possible calculate the four intersection points for the ground plane. For that the *Cramer's Rule* is applied. [14]

$$\text{Plane 1 : } A_1x + B_1y + C_1z + D_1 = 0$$

$$\text{Plane 2 : } A_2x + B_2y + C_2z + D_2 = 0 \quad (9)$$

$$\text{Plane 3 : } A_3x + B_3y + C_3z + D_3 = 0$$

$$x = \frac{\text{Det}_{DBC}}{\text{Det}_{ABC}} \quad y = \frac{\text{Det}_{ADC}}{\text{Det}_{ABC}} \quad z = \frac{\text{Det}_{ABD}}{\text{Det}_{ABC}} \quad (10)$$

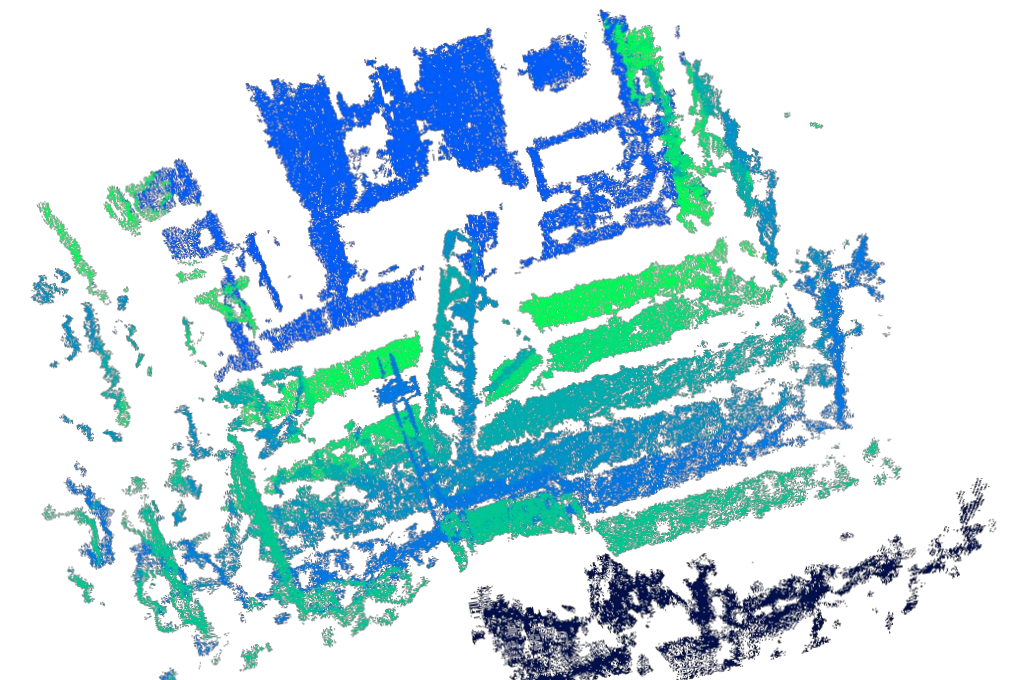
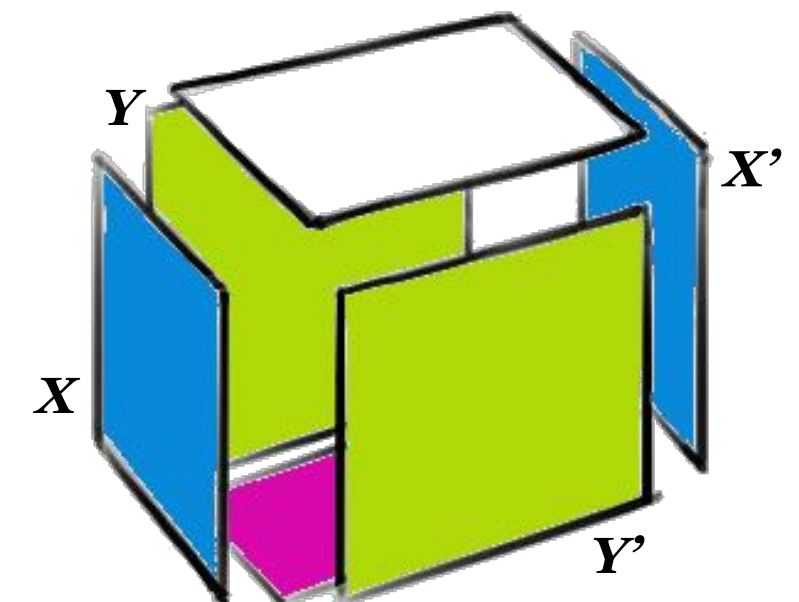


Figure 19. Segmented planes on the  $y$ -coordinate.

## ⚙ 5. Experiments

**Objective:** Analytical calculation of the ground plane limits by wall planes intersection.

- Given the planes  $X, X', Y$  and  $Y'$ , it is possible calculate the four intersection points for the ground plane. For that the *Cramer's Rule* is applied. [14]

$$\text{Plane 1 : } A_1x + B_1y + C_1z + D_1 = 0$$

$$\text{Plane 2 : } A_2x + B_2y + C_2z + D_2 = 0 \quad (9)$$

$$\text{Plane 3 : } A_3x + B_3y + C_3z + D_3 = 0$$

$$x = \frac{\text{Det}_{DBC}}{\text{Det}_{ABC}} \quad y = \frac{\text{Det}_{ADC}}{\text{Det}_{ABC}} \quad z = \frac{\text{Det}_{ABD}}{\text{Det}_{ABC}} \quad (10)$$

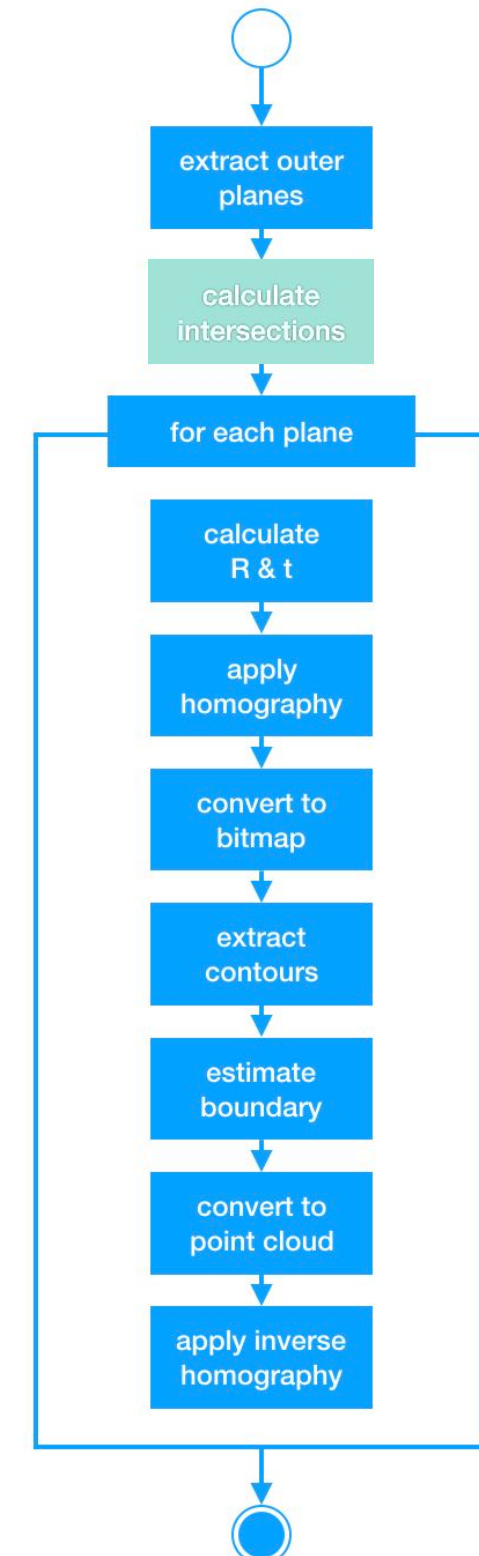


**Figure 20.** Flow chart of the algorithm.

## ⚙ 5. Experiments

**Objective:** Rotate and translate segmented planes to a common reference system centered at  $(o,o,o)$ .

- A ground plane  $N$  with normal  $\hat{n}=(0,0,1)$  was selected as reference to construct there the bitmap.
- Each segmented plane  $P$  provide a normal  $\hat{p}$ , to make the rotation and translation.

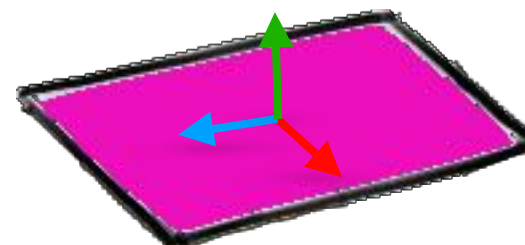


**Figure 21.** Sketch of the homography application.

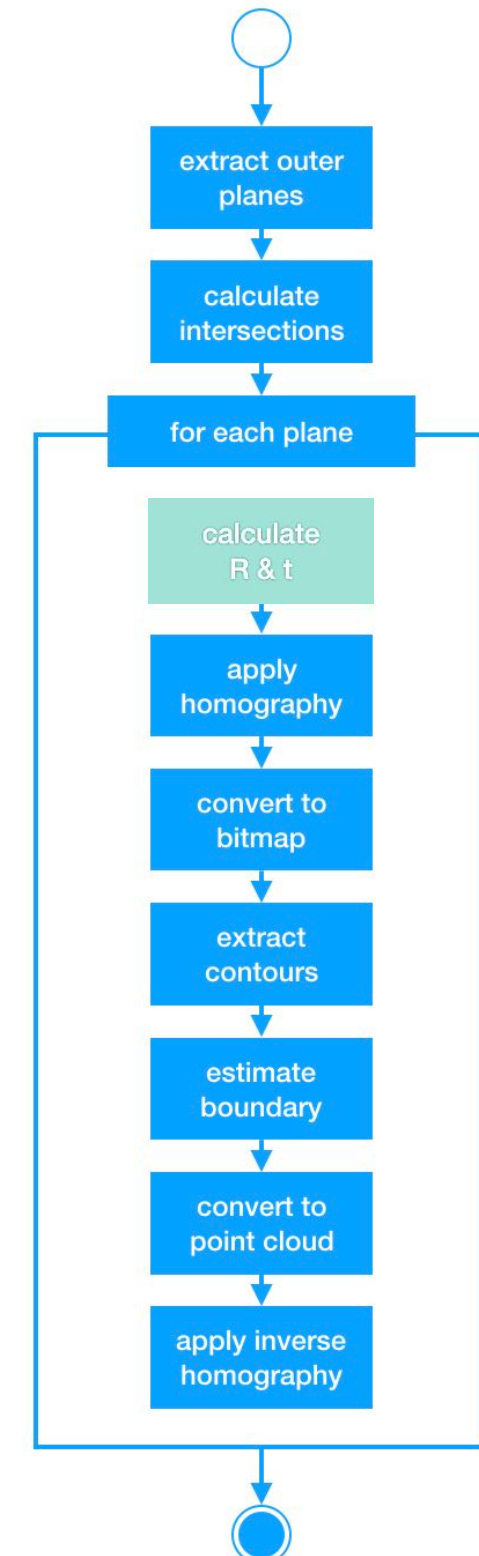


**Figure 20.** Flow chart of the algorithm.

## ⚙️ 5. Experiments

**Objective:** Rotate and translate segmented planes to a common reference system centered at  $(o,o,o)$ .

- From *Euler-Rodrigues Formula*, to rotate a unit vector  $a$  into  $b$ , simply is needed to rotate  $a$  by  $\pi$  around  $(a+b)/2$ : [15]

$$R = 2 \frac{(a + b)(a + b)^T}{(a + b)^T(a + b)} - I. \quad (11)$$

- The translation vector  $t$  is calculated as the difference between the center of mass of both planes  $N$  and  $P$ . Hence, is composed the homography  $H$  given in Equation 2:

$$X' = H_E X = \begin{bmatrix} R & t \\ 0^T & 1 \end{bmatrix}$$

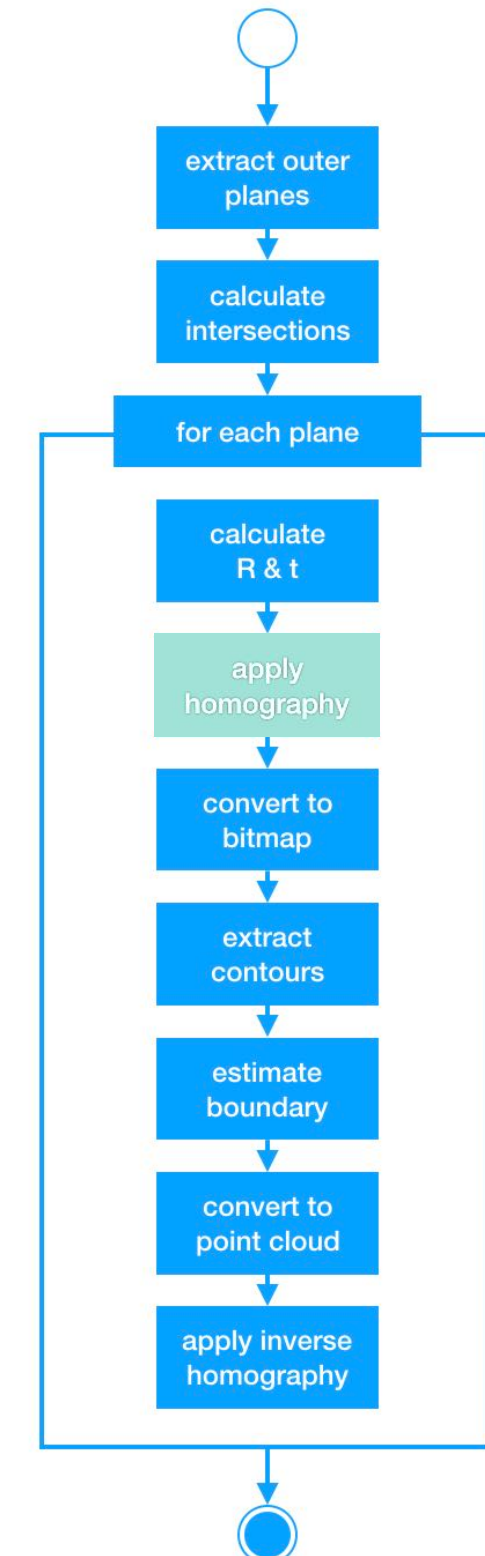


**Figure 20.** Flow chart of the algorithm.

## ⚙ 5. Experiments

**Objective:** Create the bitmap of the projected plane centered at  $(o,o,o)$ .

- The orthogonal projection of each point on the reference plane (i.e. XY) lies directly in the coordinate  $(x, y)$  where  $z = o$ .

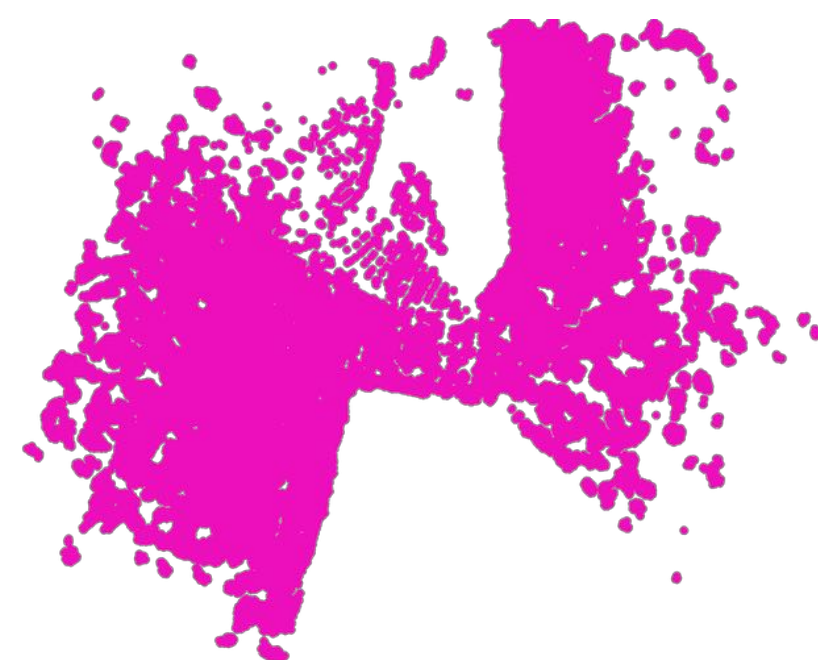


**Figure 22.** Sketch of the bitmap conversion.

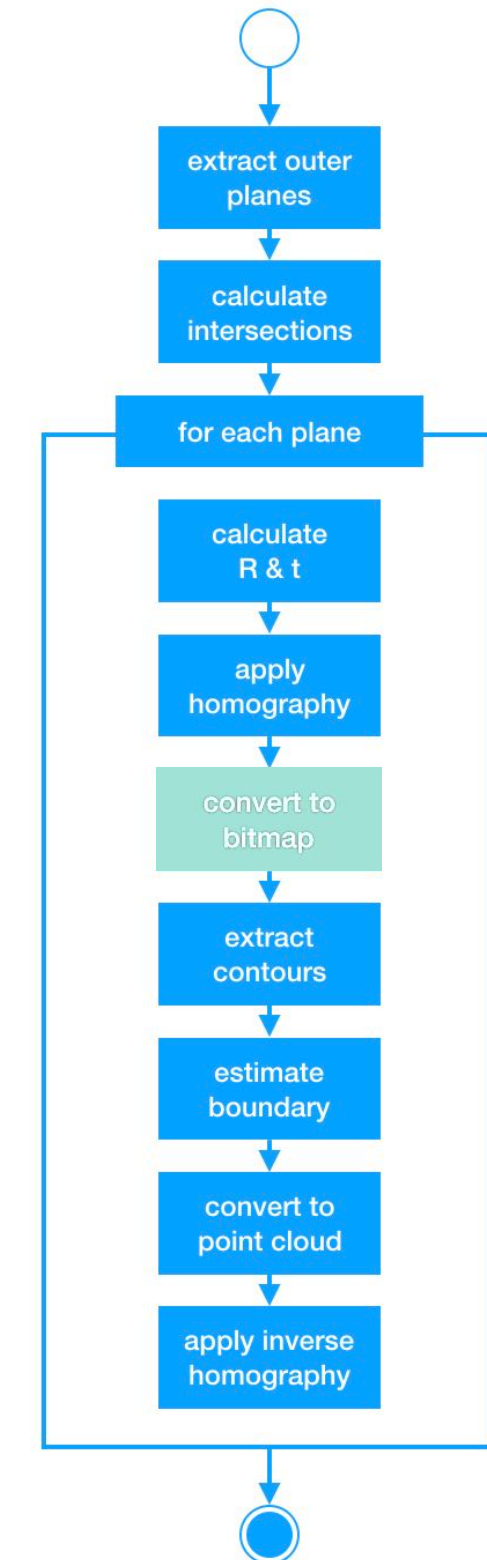


**Figure 20.** Flow chart of the algorithm.

## ⚙️ 5. Experiments

- The orthogonal projection of each point on the reference plane (i.e. XY) lies directly in the coordinate  $(x, y)$  where  $z = 0$ .

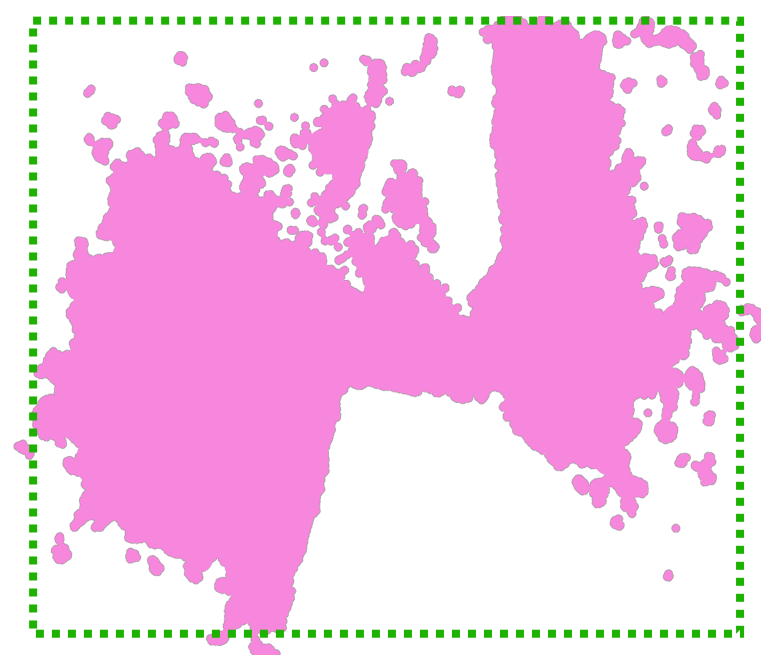


**Figure 23.** Sketch of the contour extraction.

- The *closing* of the image is applied making use of a rectangular structuring element.

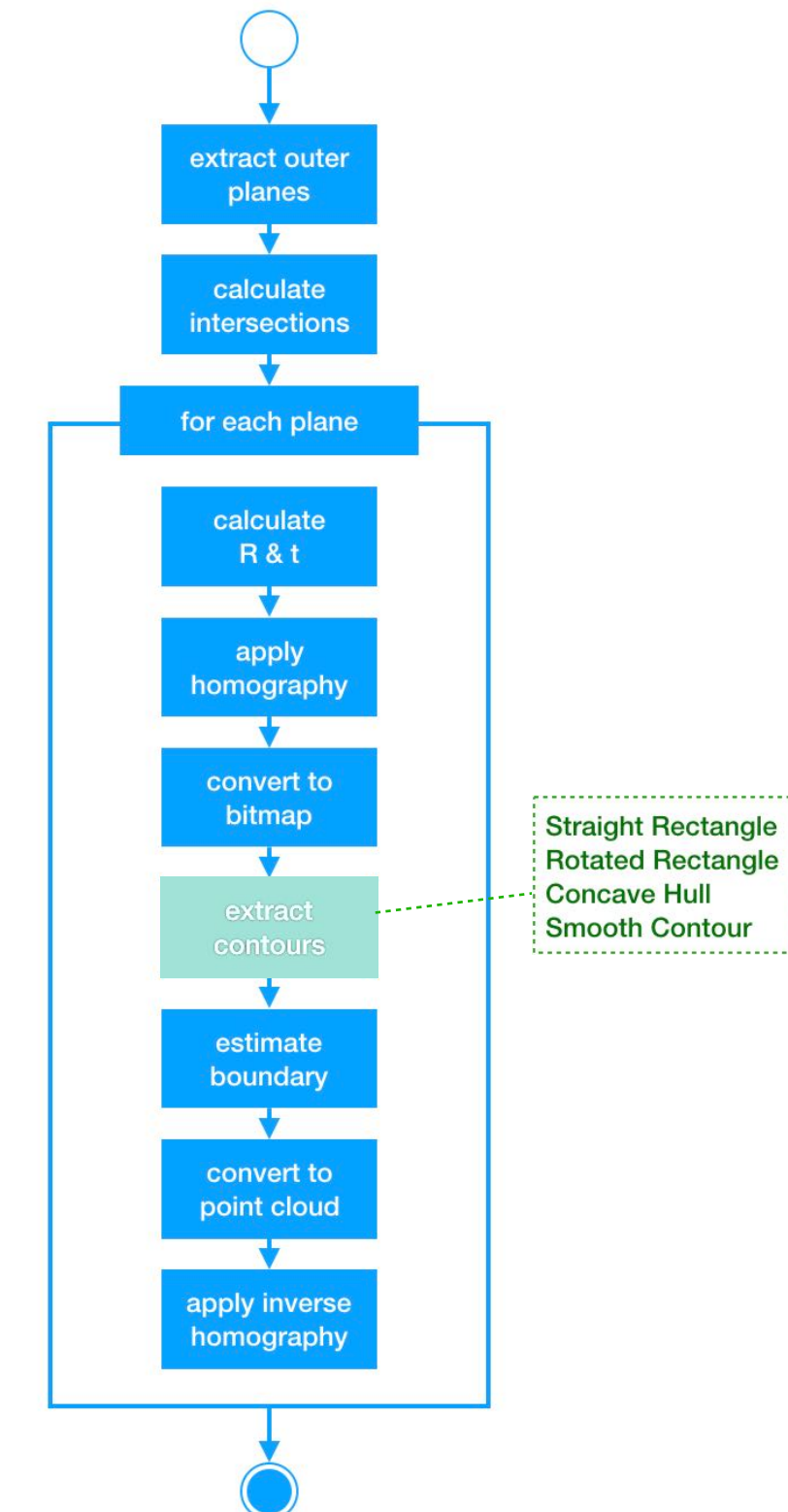


**Figure 20.** Flow chart of the algorithm.

## ⚙️ 5. Experiments

- The orthogonal projection of each point on the reference plane (i.e. XY) lies directly in the coordinate  $(x, y)$  where  $z = 0$ .

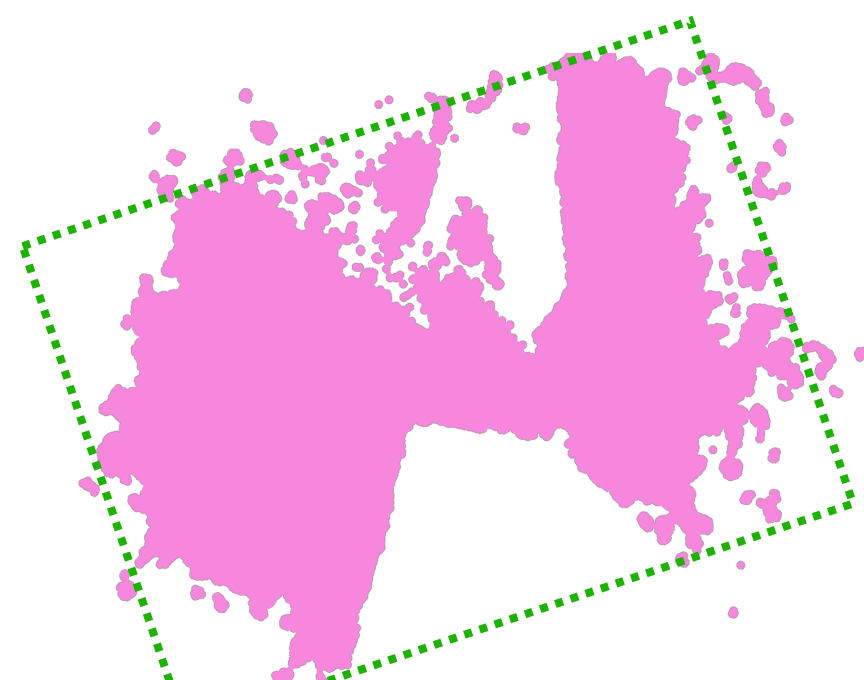


**Figure 23.** Sketch of the contour extraction.

- The *closing* of the image is applied making use of a rectangular structuring element.

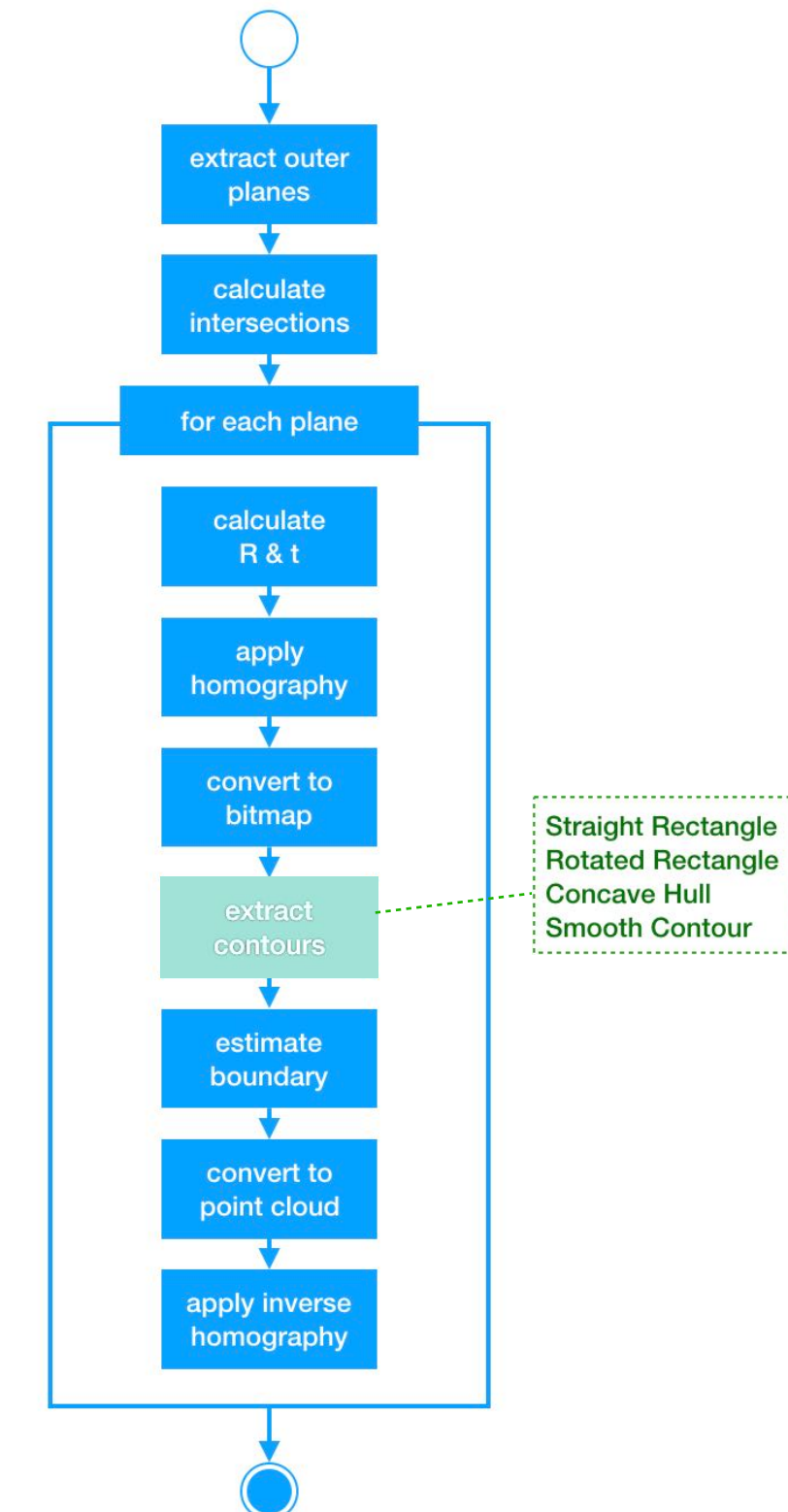


**Figure 20.** Flow chart of the algorithm.

## ⚙ 5. Experiments

- The orthogonal projection of each point on the reference plane (i.e. XY) lies directly in the coordinate  $(x, y)$  where  $z = 0$ .

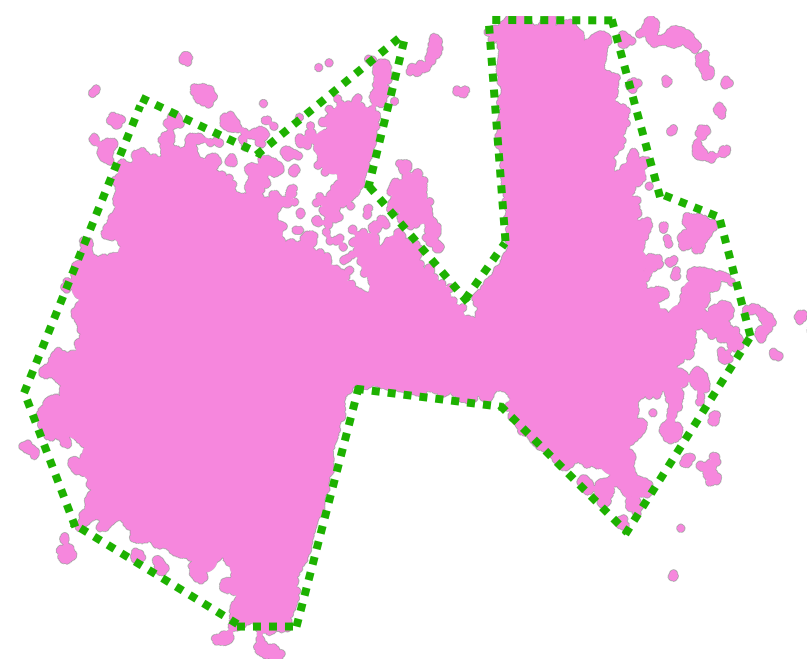


**Figure 23.** Sketch of the contour extraction.

- Detect boundaries finding curves with the fewer possible points, by 'dissimilar' distance between an original curve and the simplified one. [16]

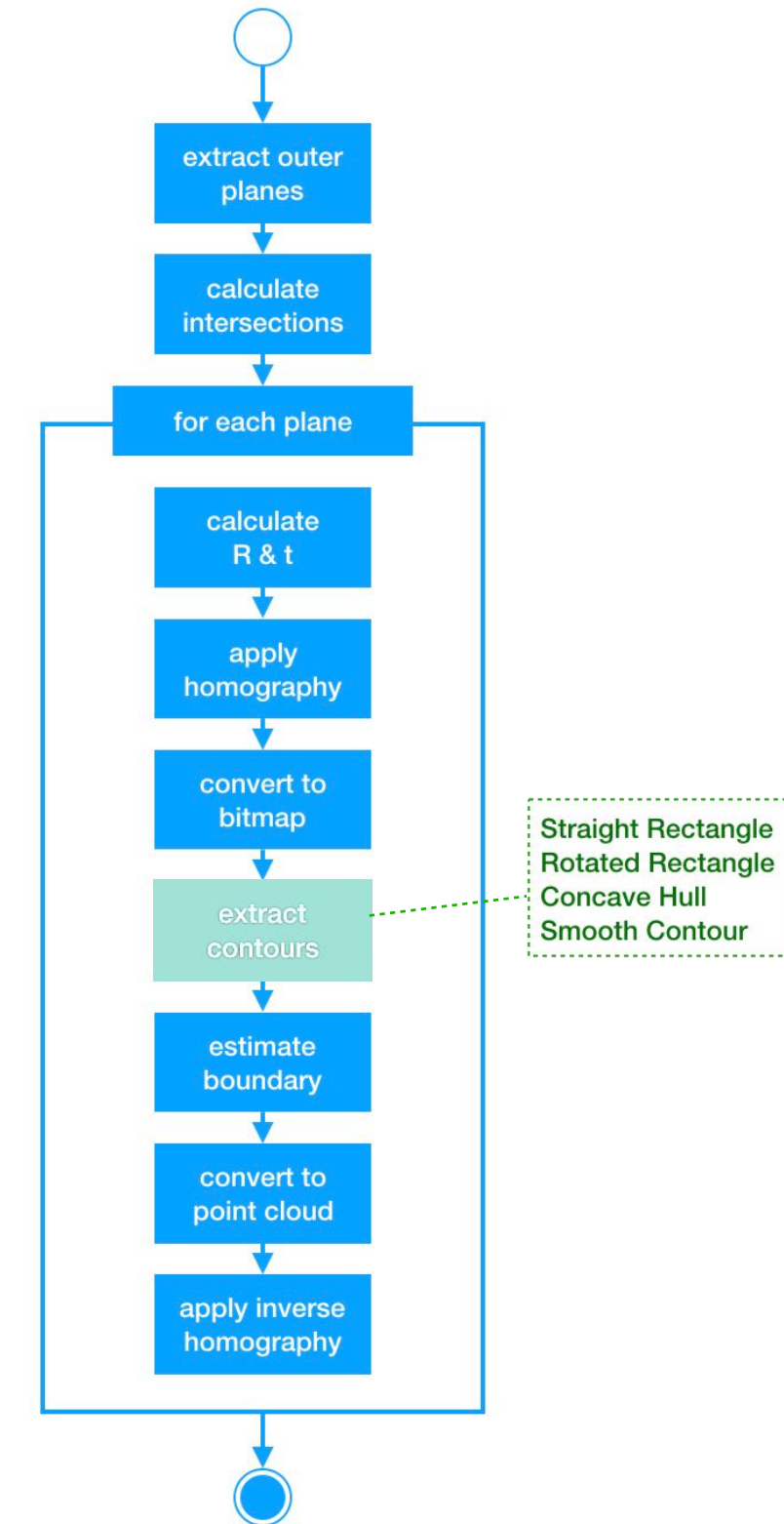


**Figure 20.** Flow chart of the algorithm.

## ⚙ 5. Experiments

- The orthogonal projection of each point on the reference plane (i.e. XY) lies directly in the coordinate  $(x, y)$  where  $z = 0$ .

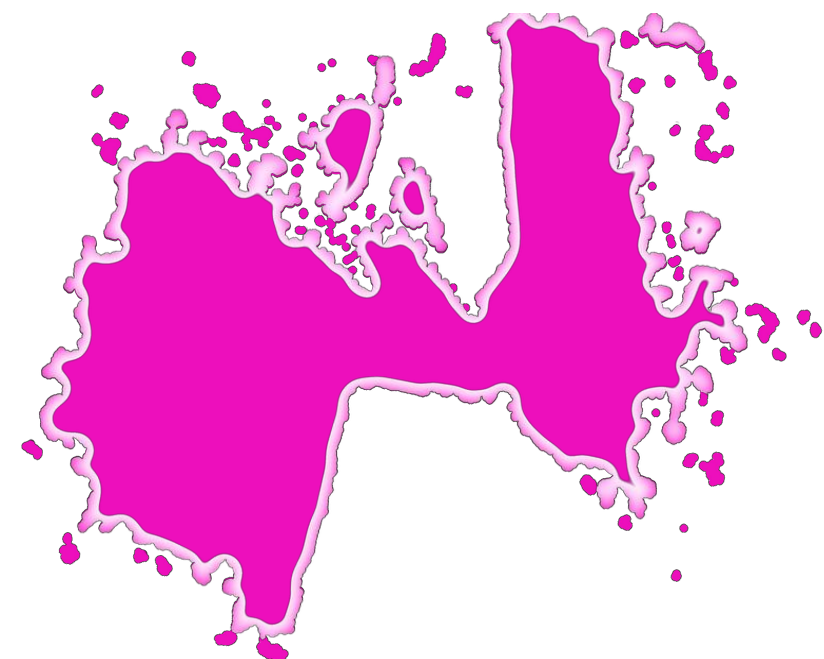


**Figure 23.** Sketch of the contour extraction.

- Detect boundaries finding curves with the fewer possible points, by 'dissimilar' distance between an original curve and the simplified one. [16]

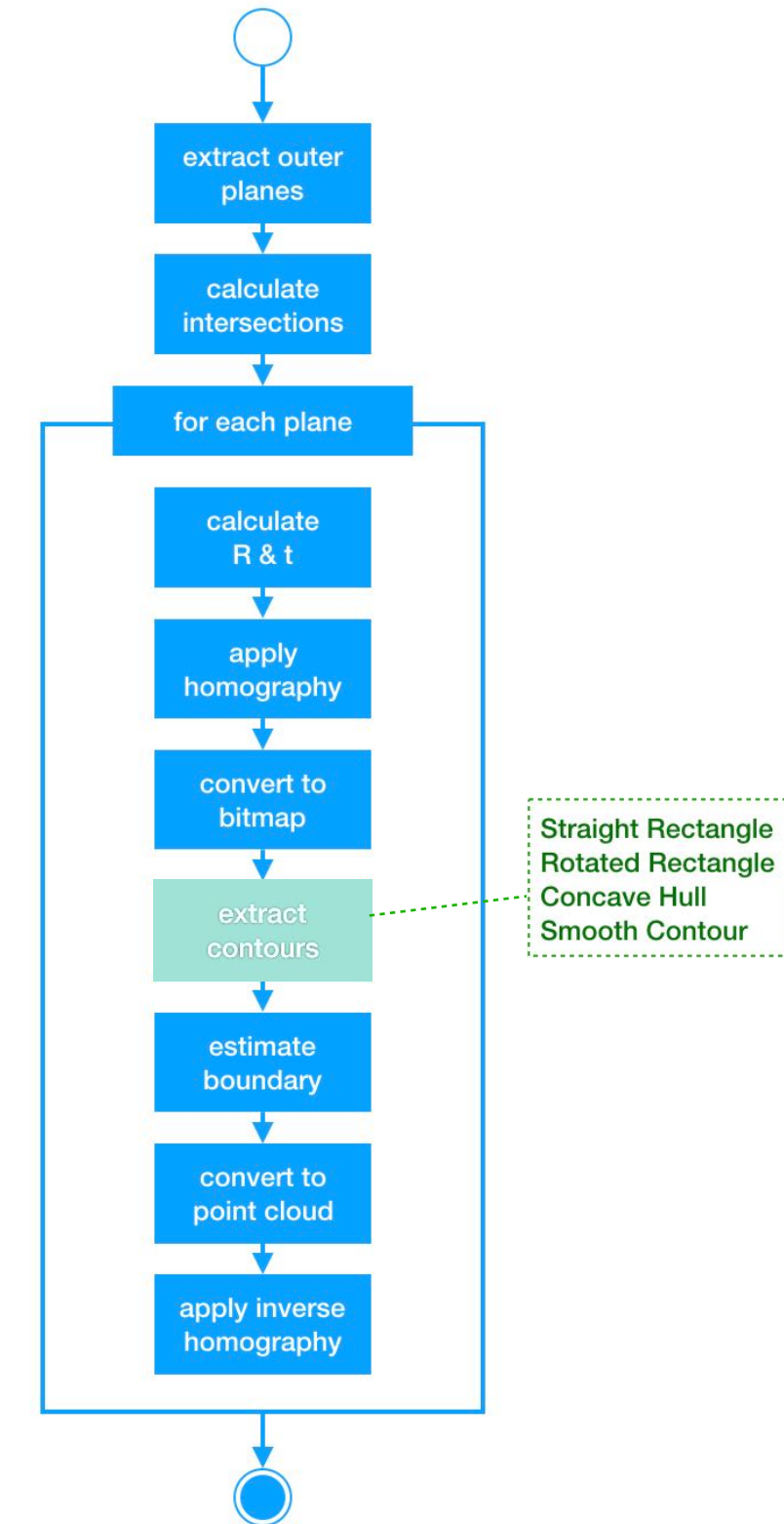


**Figure 20.** Flow chart of the algorithm.

## ⚙ 5. Experiments

- One approximation is to continue with the image dilation increasing the size of the structuring element; disadvantage, it produces blurring borders.

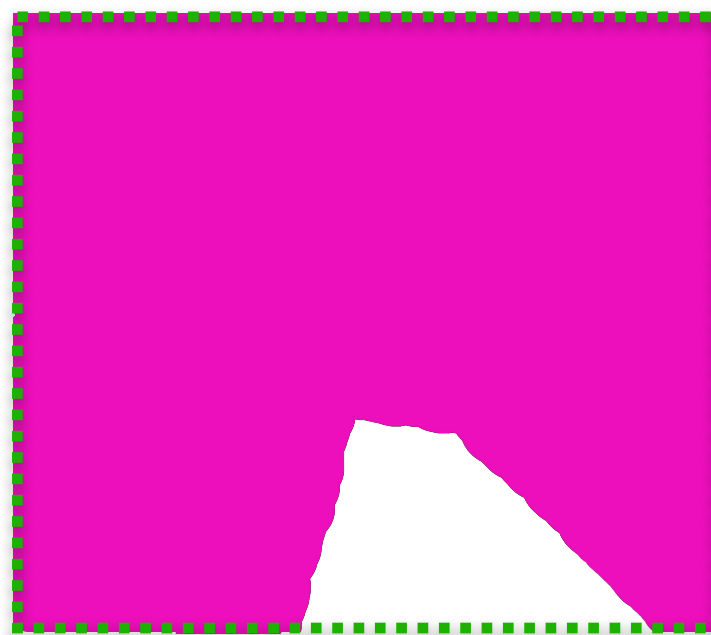


**Figure 24.** Sketch of the boundary estimation.

- To limit the expansion of the dilation it is used the calculated analytical borders with Equation 10.

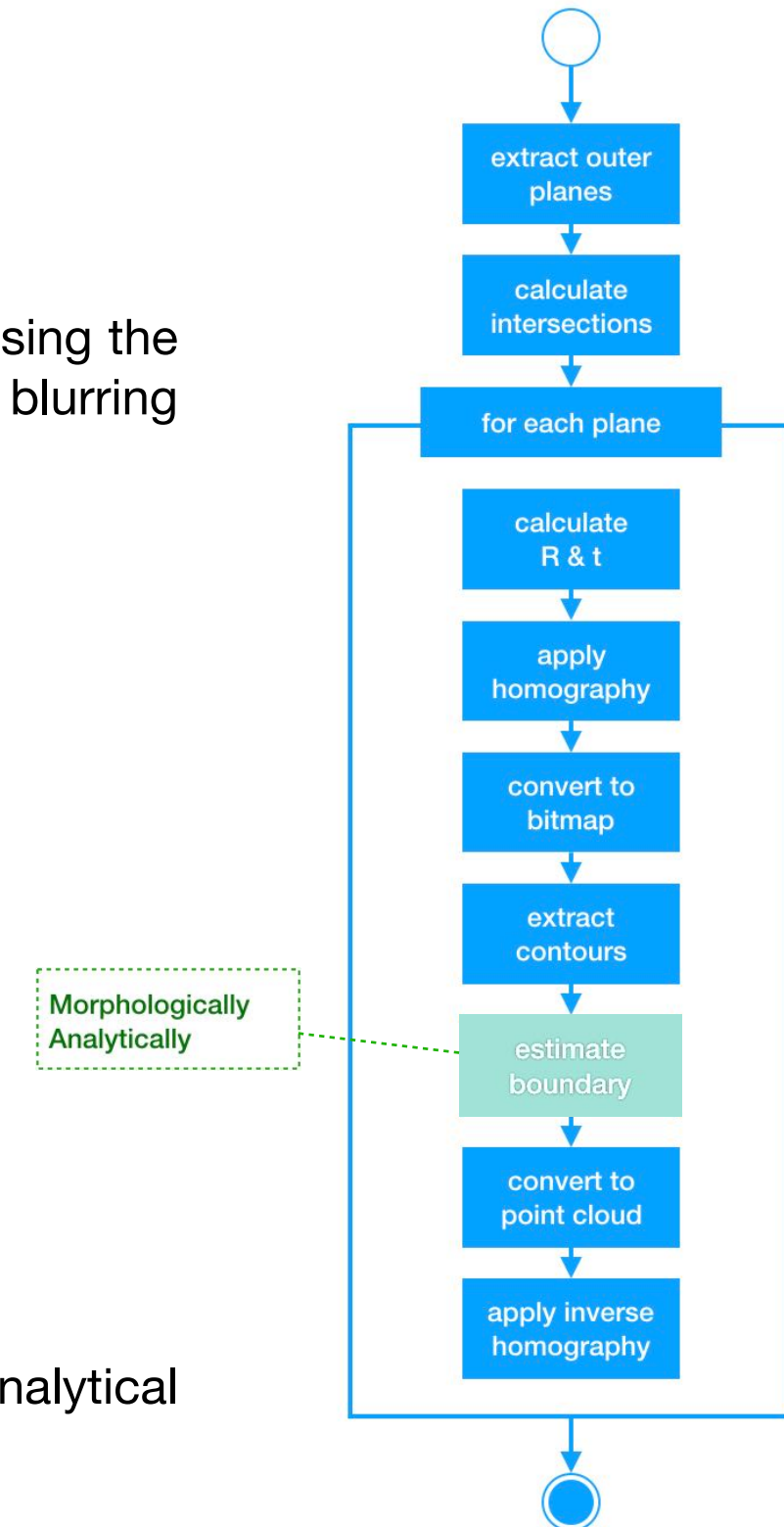


**Figure 20.** Flow chart of the algorithm.

## ⚙️ 5. Experiments

- On the plane XY and with the image centroid at  $(0,0,0)$ , to convert the bitmap to a point cloud, the pixels are projected perpendicularly from the plane assigning a value for the z-coordinate within an interval or *depth*.



**Figure 25.** Sketch of the point cloud conversion.

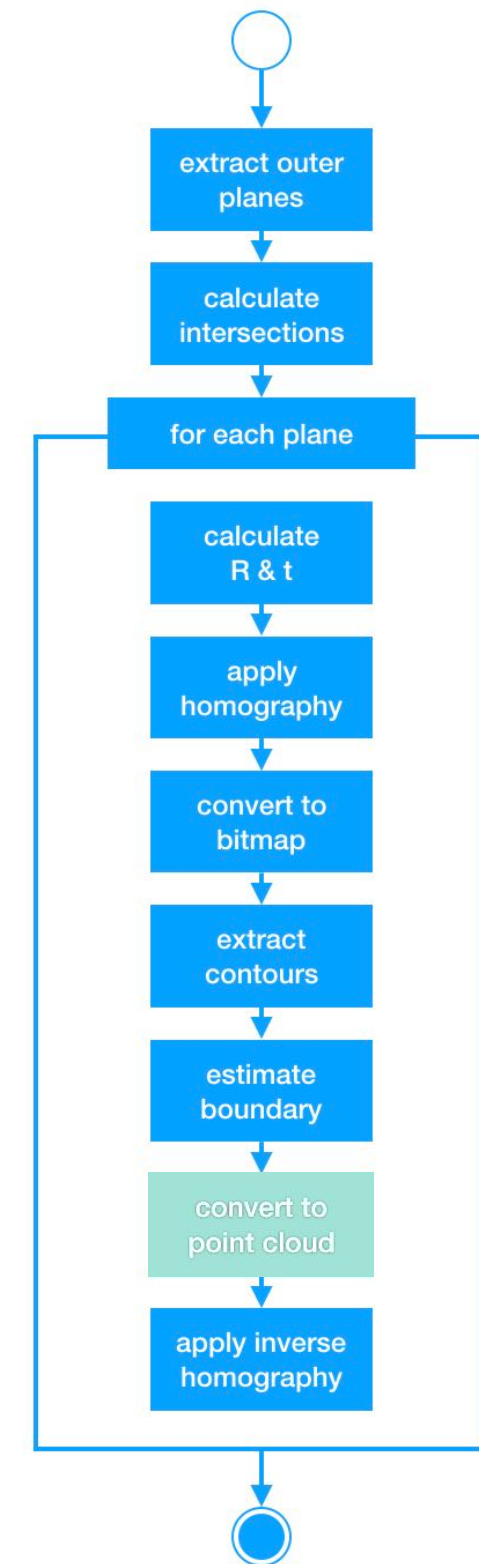


**Figure 20.** Flow chart of the algorithm.

## ⚙ 5. Experiments

- On the plane XY and with the image centroid at  $(0,0,0)$ , to convert the bitmap to a point cloud, the pixels are projected perpendicularly from the plane assigning a value for the z-coordinate within an interval or *depth*.

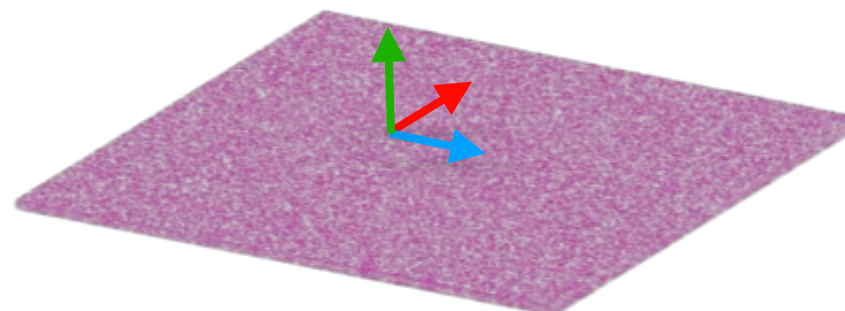


**Figure 25.** Sketch of the point cloud conversion.

- Not all the pixels can be transformed. It is required to establish a *density* to describe the points per unit area. The calculation of z value, as well as the pixel selection  $(x,y)$ , use the Normal Distribution.

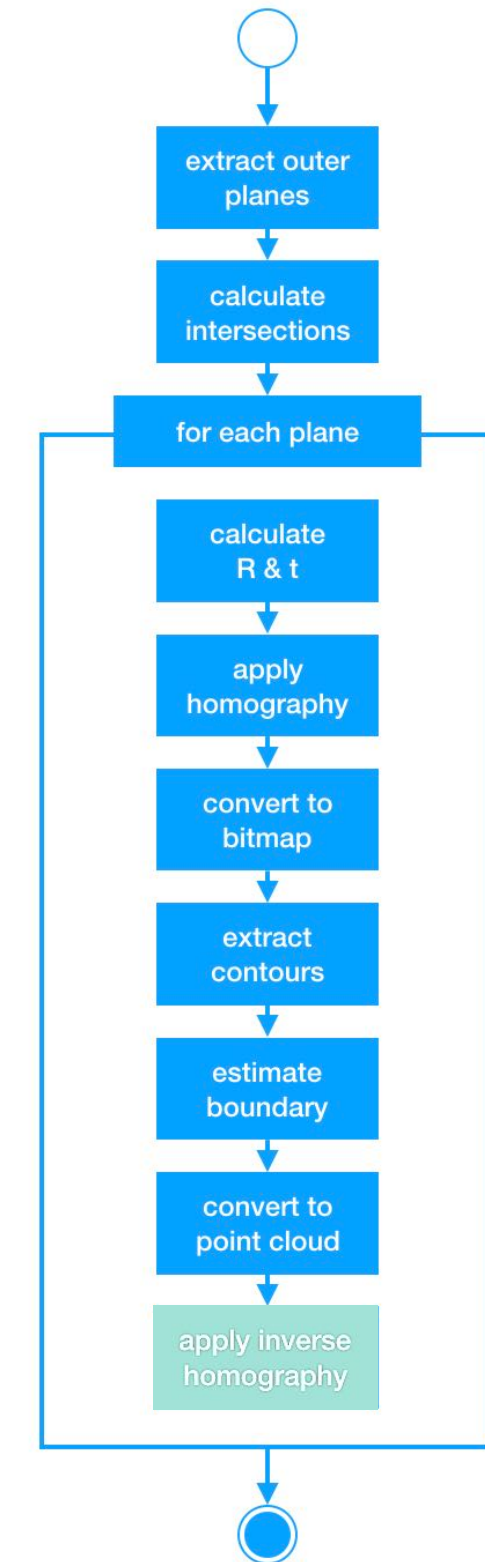


**Figure 20.** Flow chart of the algorithm.



## 6. Results

- Optimum values for the parametric threshold variables  $d$  and  $\varepsilon$  in RANSAC, after the iterative extraction across each coordinate  $x$ ,  $y$  and  $z$ .

Testing ranges:  $60 \leq d \leq 150 \text{ mm}$  step  $10 \text{ mm}$   
 $4^\circ \leq \varepsilon < 20^\circ$  step  $3^\circ$

Area ( $\text{mm}^2$ )	9989012
Width ( $\text{mm}$ )	1733
Height ( $\text{mm}$ )	5764
Depth ( $\text{mm}$ )	264
MassC( $x,y,z$ )	-2306,778,991

Area	10606860
Width	1980
Height	5357
Depth	247
MassC	445,-213,1145

Area	4184992
Width	784
Height	5338
Depth	266
MassC	-1322,32,1028

Area	2816730
Width	714
Height	3945
Depth	253
MassC	1782,490,989

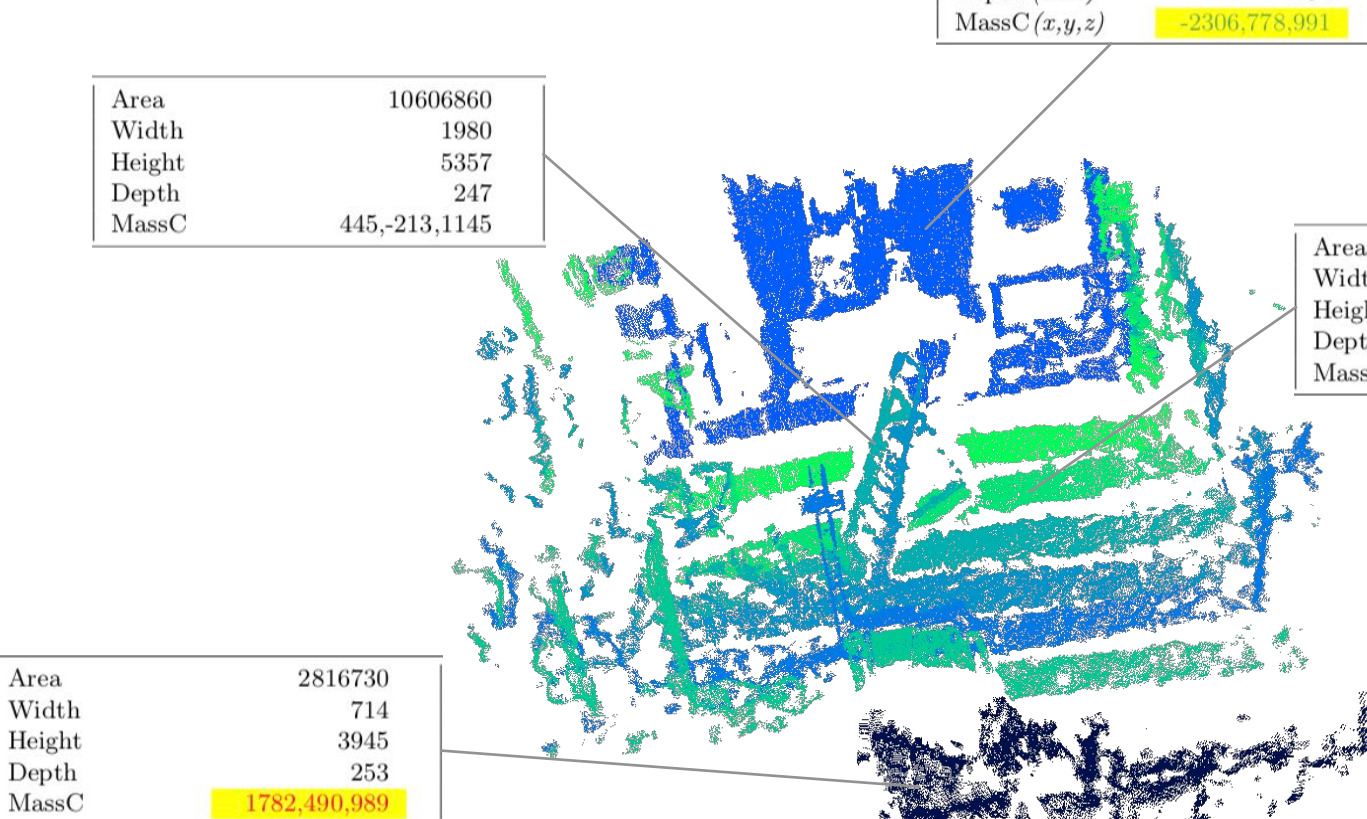


Figure 19. Segmented planes on the  $y$ -coordinate.



## 6. Results

- Optimum values for the parametric threshold variables  $d$  and  $\varepsilon$  in RANSAC, after the iterative extraction across each coordinate  $x$ ,  $y$  and  $z$ .
- Using a 3D-Cartesian coordinate system centered at  $(0,0,0)$ , taking the maximum and minimum position on each axis, the optimum values were:

coordinate angle ( $d$ )	$x$	$y$	$z$
thr_dis ( $\varepsilon$ )	$19^\circ$ $150\text{mm}$	$19^\circ$ $150\text{mm}$	$19^\circ$ $150\text{mm}$

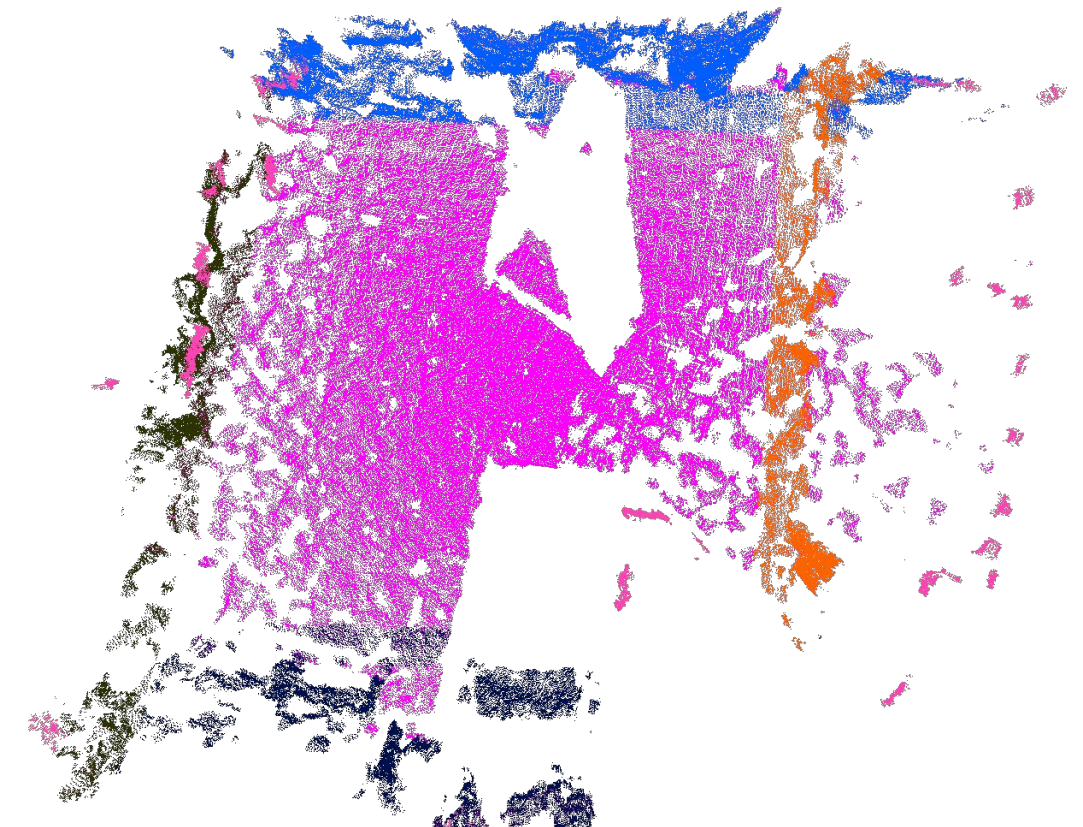


**Figure 26.** Best choice for parameters introduced in the segmentation.



## 6. Results

- The determination of the bounding box for a given region depends more on the quality of the point cloud, i.e. the density and its distribution.
- Comparison of areas enclosed by the available bounding box methods applied to one wall plane:

Plane ID		Bounding Area	Percent.
1-0-0	a) Straight Rectangle (SE 50 mm)	8828591 mm <sup>2</sup>	88%
	b) Rotated Rectangle (SE 50 mm)	8328483 mm <sup>2</sup>	83%
	c) Concave Hull (SE 120 mm)	6753426 mm <sup>2</sup>	68%
	d) Smooth Contour (SE 10 mm)	7446628 mm <sup>2</sup>	75%
Enclosing Box		9989012 mm <sup>2</sup>	100%

A rectangular structuring element (SE) were used with different sizes. The percentages show the area into the dashed lines wrt. the global enclosing box. **Although the techniques (a) and (b) cover more area, (c) and (d) are more accurate with the image shape.**

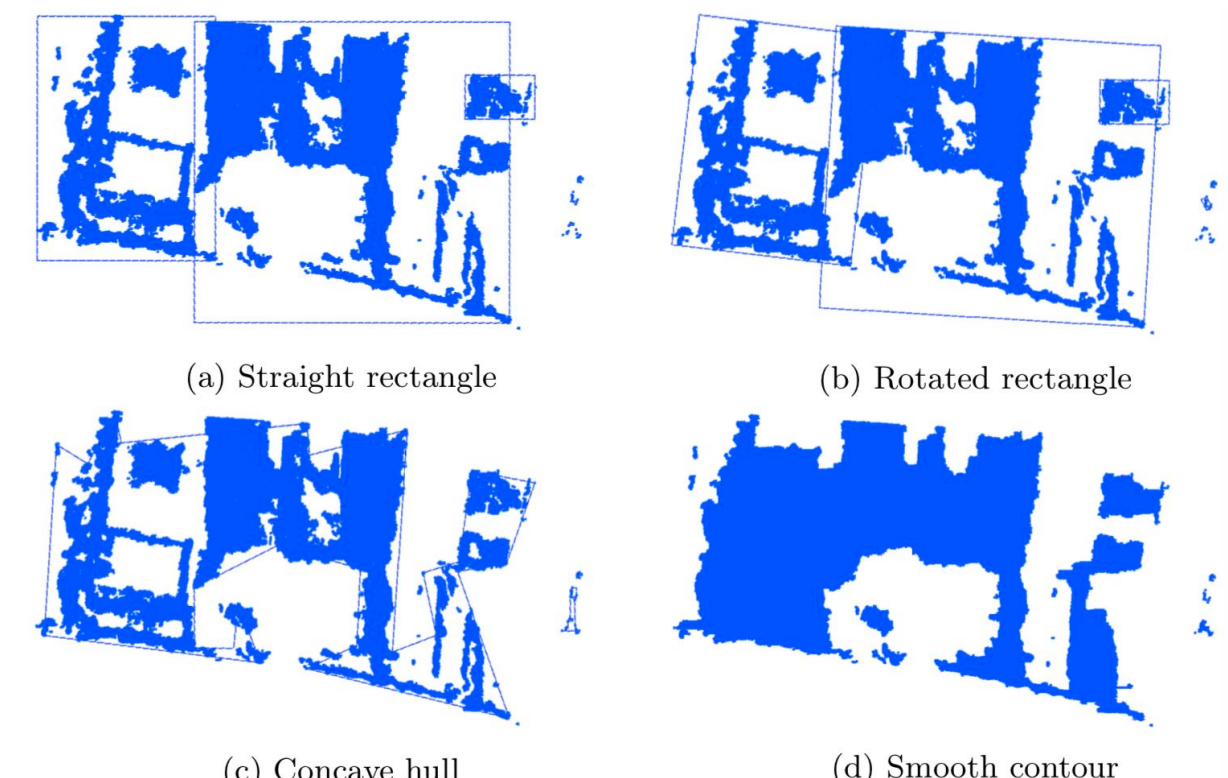
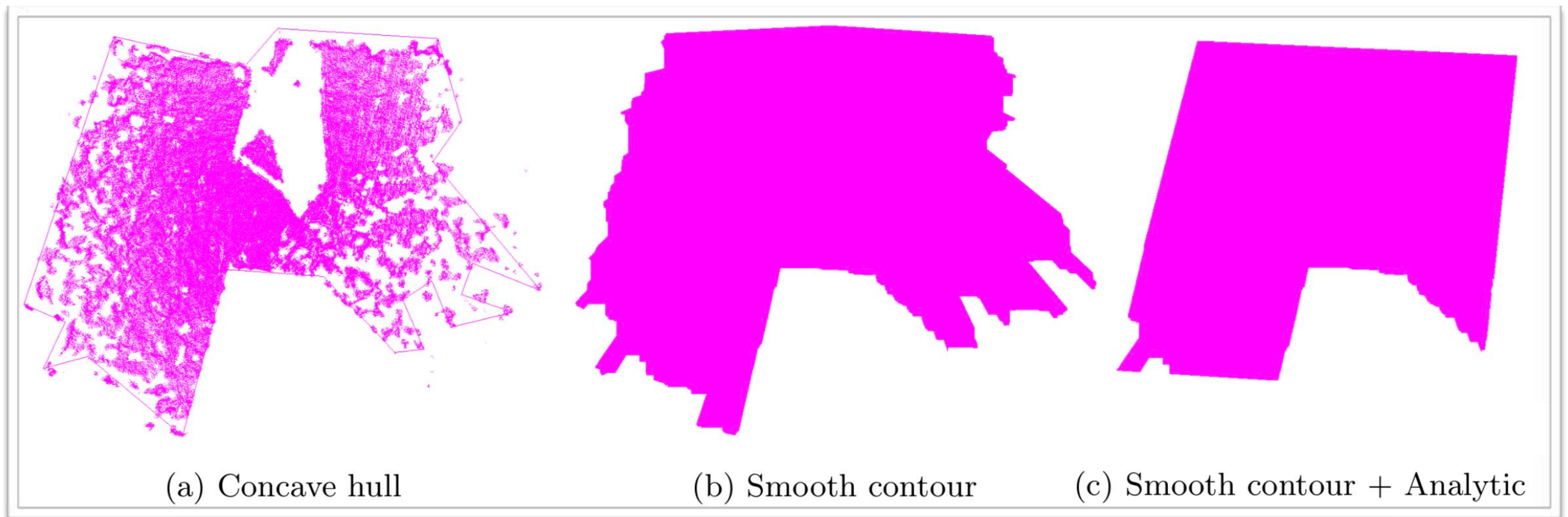


Figure 27. Bounding box estimation for the first plane in YZ.



- Concave Hull and Smooth Contour were selected as the bounding boxes that better estimate the ground silhouette:



**Figure 28.** Bounding box estimation for the ground plane.

- The analytic square estimated previously was used to filter the noise beyond the walls, hence both shapes were intersected.



## 6. Results

- Bounding boxes methods applied to the ground plane:

Plane ID		Bounding Area	Percent.	Noise	Percent. Clean
0_0_1	a) Concave Hull (SE 120 mm)	26558717 mm <sup>2</sup>	66%	13%	
	b) Smooth Contour (SE 120 mm)	27717072 mm <sup>2</sup>	69%	13%	
	c) S.Contour + Analytic (SE 120 mm)	20123685 mm <sup>2</sup>	50%	13%	58%
	d) Analytic Area	24216870 mm <sup>2</sup>	60%	13%	69%
	e) Synthetic A. – Notch	28000000 mm <sup>2</sup>	70%	0%	80%
	f) Synthetic Area	34952016 mm <sup>2</sup>	87%	0%	100%
Enclosing Box		40178691 mm <sup>2</sup>	100%		
Real Area		35000000 mm <sup>2</sup>			100%

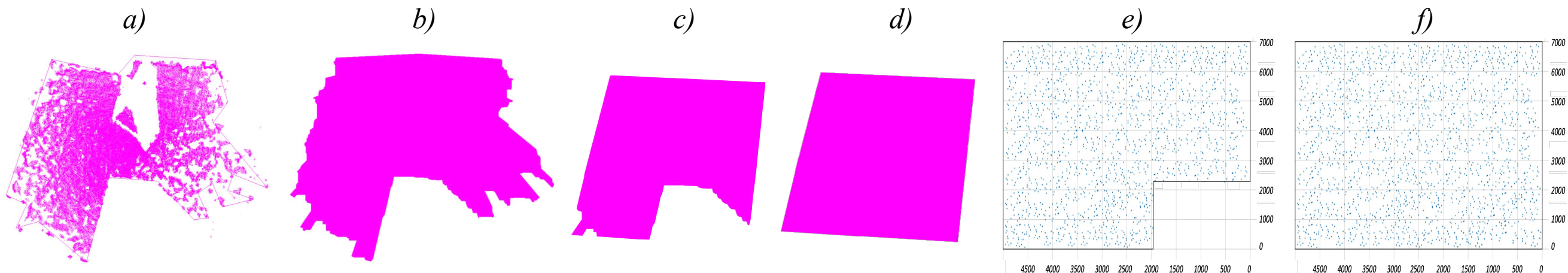


Figure 29. Comparison of the bounding boxes for the ground plane.



## 6. Results

- Bounding boxes methods applied to the ground plane:

Plane ID		Bounding Area	Percent.	Noise	Percent. Clean
0_0_1	a) Concave Hull (SE 120 mm)	26558717 mm <sup>2</sup>	66%	13%	
	b) Smooth Contour (SE 120 mm)	27717072 mm <sup>2</sup>	69%	13%	
	c) S.Contour + Analytic (SE 120 mm)	20123685 mm <sup>2</sup>	50%	13%	58%
	d) Analytic Area	24216870 mm <sup>2</sup>	60%	13%	69%
	e) Synthetic A. – Notch	28000000 mm <sup>2</sup>	70%	0%	80%
	f) Synthetic Area	34952016 mm <sup>2</sup>	87%	0%	100%
Enclosing Box		40178691 mm <sup>2</sup>	100%		
Real Area		35000000 mm <sup>2</sup>			100%

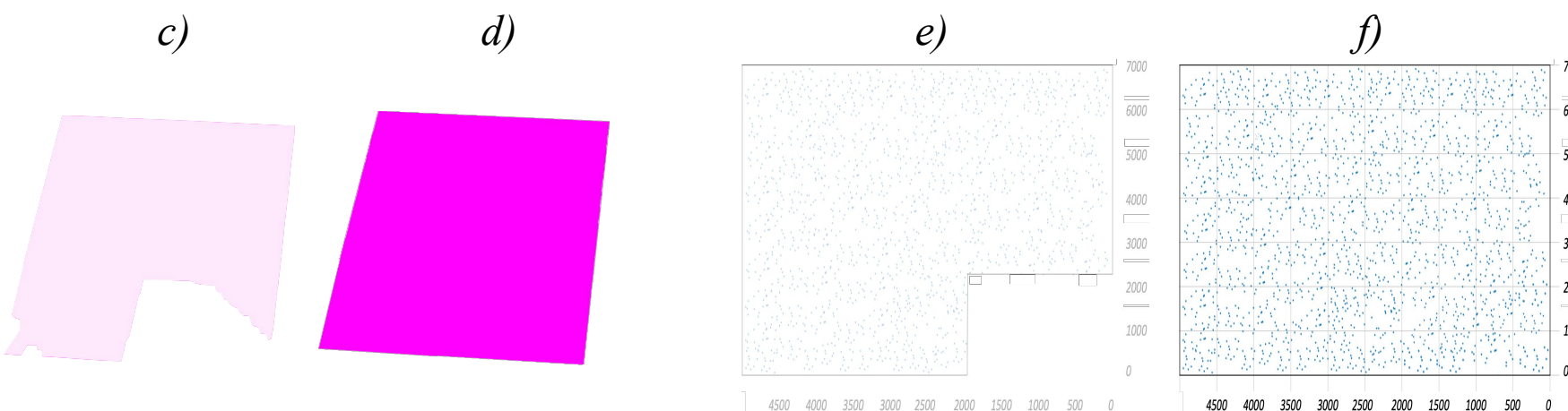


Figure 30. Comparison of the bounding boxes for the ground plane.

The relation ‘S. Contour + Analytic’ vs. ‘Analytic Area’ gives a ratio of **83%**.

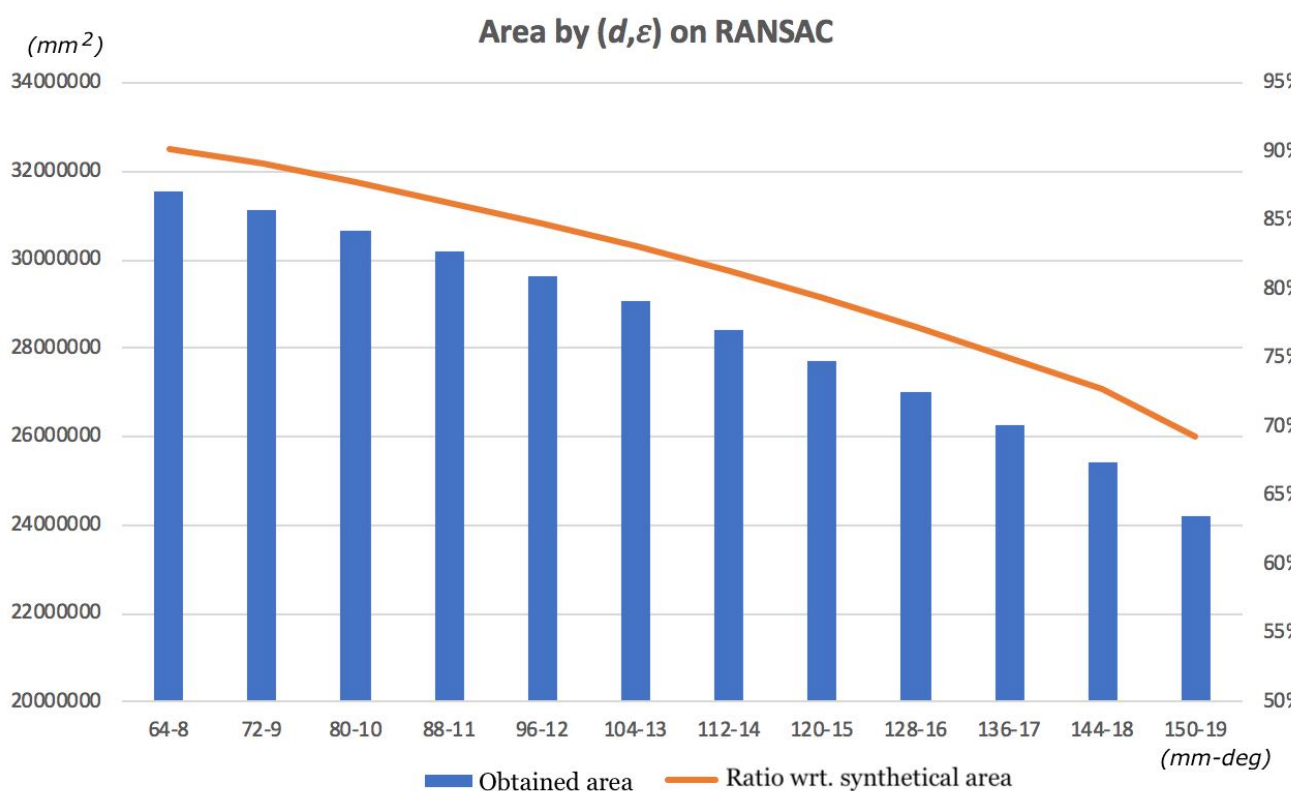
The ratio for the real scenario (‘Synthetic A. - Notch’ vs. ‘Synthetic Area’) presents **80%**.

The deviation between the complete areas, was **31%**. Due to the RANSAC parameters taken for the analytic one:

$$d = 150\text{mm} \quad \text{and} \quad \varepsilon = 19^\circ.$$

## ❖ 7. Evaluation and Outlook

- Into the plane segmentation the selection of the tuple  $(d,\varepsilon)$  represents losses ranging from  $2d$  to  $h_w/2 \cdot \sin \varepsilon$  per ground side, being  $h$  the wall height.



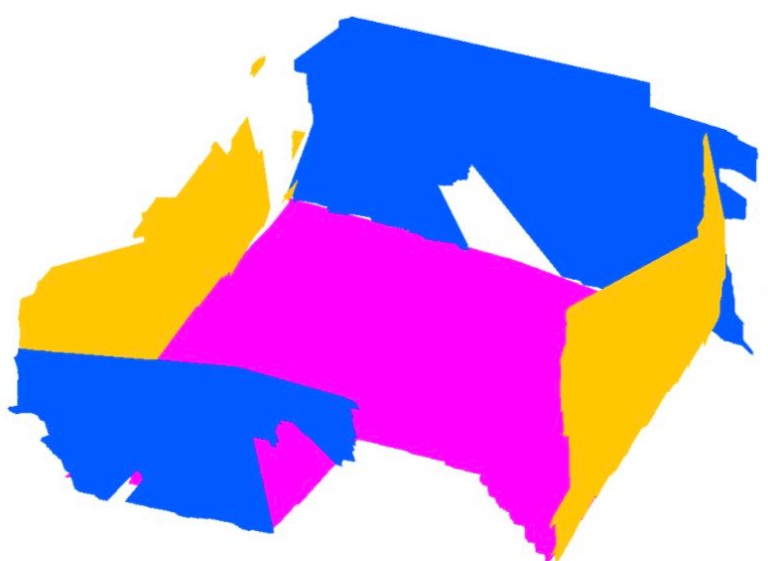
- 90 plane extraction in total were performed.
- The lower wall thickness (and inclination) the bigger ground plane area.

**Figure 31.** Ground plane area calculation for 12 different RANSAC parameters.

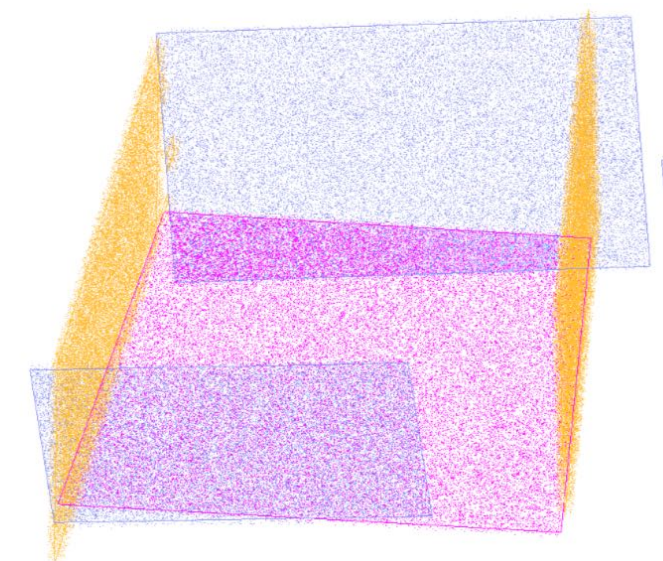
- With a nearness of **90%**, the most accurate area for the ground plane is given with  $d=64$  and  $\varepsilon=8$  (in detriment of walls detection).

## ❖ 7. Evaluation and Outlook

**Objective:** The complete fit in of the plane into the boundaries given by the walls, as the synthetic construction.



(a) Bitmap of erosion



(b) Back-transformation of point cloud  
reconstructed

- Ground plane reconstructed with analytical assumptions.
- Back-transformation from 2D to 3D using an uniform distribution.

**Figure 32.** Final result after bitmap to point cloud conversion, with a density of 30 points per  $cm^3$ .

- Problems with the normals which produce wrong rectangular boundaries detection.

## ❖ 7. Evaluation and Outlook

- Some methods offer detailed modelling of small scenes and others are aimed at larger scenes but with few details, however there is no method that encompasses detailed reconstruction on a large scale. [17]
- Current techniques have practical applications and the continuous research produces every day many options to solve complex digitalization tasks, such as target and tracking small objects in an indoor scene.
- The field of application is increasing, as well as the opportunities to develop useful products for people inside homes and offices, which is an encouraging scenario to continue the research in this area.



## 8. References

- [1] Hisato Kawaji, Koki Hatada, Toshihiko Yamasaki and Kiyoharu Aizawa. Image-based indoor positioning system: Fast image matching using omnidirectional panoramic images. 1st ACM international workshop on Multimodal pervasive video analysis, pages 1-4, 2010.
- [2] Michel Findeisen and Gangolf Hirtz. Trinocular spherical stereo vision for indoor surveillance. Canadian Conference on Computer and Robot Vision (CRV), pages 364–370, 2014.
- [3] Sundaresh Ramakrishnaiah. 3D plane estimation in point cloud. Research Project, professorship of Digital Signal Processing and Circuit Design, TU-Chemnitz, 2017.
- [4] Emiliano Pérez. Técnicas de Relleno de Huecos en Superficies Adquiridas Mediante Escáneres 3D. PhD thesis, Universidad Nacional de Educación a Distancia, Extremadura, España, 2011.
- [5] Paul Bourke. Omni-directional Stereoscopic Fisheye Images for Immersive Hemispherical Dome Environments. Proceedings of the Computer Games & Allied Technology 09, Singapore, May 12, 2009
- [6] Remus Dumitru, Dorit Borrmann and Andreas Nüchter. Interior reconstruction using the 3D Hough transform. International Archives of the Photogrammetry, Remote Sensing and Spatial Information Sciences, XL-5/W1(3D-ARCH 2013), February 2013. Trento, Italy.
- [7] Bastian Oehler, Jörg Stückler, Jochen Welle, Dirk Schulz and Sven Behnke. Efficient multi-resolution plane segmentation of 3D point clouds. 4th International Conference Intelligent Robotics and Applications ICIRA, pages 145–156, December 2011.
- [8] Giuseppe Papari and Nicolai Petkov. Edge and line oriented contour detection: State of the art. Image and Vision Computing, 29(2-3):79–103, February 2011.
- [9] Manuel Forero, Camila Merchan and Camilo Murillo. Analysis of binarisation techniques based on 2D histograms. Rev. Ingeniería: Ciencia, Tecnología e Innovación, 3(2):24–34, September 2016.



## 8. References

- [10] Kwanghee Ko and Takis Sakkalis. Orthogonal projection of points in CAD/CAM applications: an overview. *Journal of Computational Design and Engineering*, 1(2):116–127, February 2014.
- [11] Richard Hartley and Andrew Zisserman. *Multiple View Geometry in Computer Vision*. Cambridge University Press, New York, USA, 2 edition, 2004. ISBN 13 978-0-511-18618-9 eBook (EBL).
- [12] Rafael Gozález and Richard Woods. *Digital Image Processing*. Pearson Education, Inc., New Jersey, USA, 3 edition, 2008. ISBN 0-13-168728-x 978-0-13-168728-8.
- [13] Hoang Nguyen, David Belton and Petra Helmholz. A comparative study of automatic plane fitting registration for MLS sparse point clouds with different plane segmentation methods. *ISPRS Annals of the Photogrammetry, Remote Sensing and Spatial Information Sciences*, IV-2/W4, September 2017.
- [14] Erwin Kreyszig. *Advanced Engineering Mathematics*, volume 1. Limusa Wiley, México, 3 edition, 2003. ISBN 968-18-5310-5.
- [15] Nico Schlömer. Calculate rotation matrix to align vector a to vector b in 3D? Mathematics Stack Exchange, March 2018. URL: <https://math.stackexchange.com/q/2672702>. <https://math.stackexchange.com/users/36678/nico-schl%C3%b6mer>.
- [16] Prasad Dilip, Leung Maylor, Quek Chai and Cho Siu. A novel framework for making dominant point detection methods non-parametric. *Image and Vision Computing*. 30(11):843–859. 2012. doi:[10.1016/j.imavis.2012.06.010](https://doi.org/10.1016/j.imavis.2012.06.010).
- [17] Sven Oesau. Geometric modeling of indoor scenes from acquired point data. PhD thesis, Université Nice, Sophia Antipolis, 2015.